STRUCTURAL PROPERTIES OF AMP-ACTIVATED PROTEIN KINASE. DIMERIZATION, MOLECULAR SHAPE, AND CHANGES UPON LIGAND BINDING

Uwe Riek[1,2*], Roland Scholz[1], Peter Konarev[3], Arne Rufer[4], Marianne Suter[1], Alexis Nazabal[5], Philippe Ringler[6], Mohamed Chami[6], Shirley A. Müller[6], Dietbert Neumann[1], Michael Forstner[7], Michael Hennig[4], Renato Zenobi[5], Andreas Engel[6], Dmitri Svergun[3], Uwe Schlattner[2,1‡*] and Theo Wallimann[1‡]

From the [1] Institute of Cell Biology, ETH Zurich, Zurich, Switzerland, [2] Inserm, U884, Grenoble, France; Laboratory of Fundamental and Applied Bioenergetics, University Joseph Fourier, Grenoble, France, [3] EMBL, DESY, Hamburg, Germany, and Institute of Crystallography, Russian Academy of Sciences, Moscow, Russia, [4] F. Hoffmann-La Roche AG, Pharma Research Discovery Chemistry, Basel, Switzerland, [5] Analytical Chemistry, Laboratory of Organic Chemistry, ETH Zurich, Zurich, Switzerland, [6] M.E. Müller Institute for Structural Biology, University of Basel, Basel, Switzerland, and [7] Zürich Financial Services, Risk Engineering, Zurich, Switzerland.

[‡]U. Schlattner and T. Wallimann share senior authorship.

Running title: Structural properties of AMPK

*Address correspondence to: Uwe Schlattner, Inserm, U884, Laboratory of Fundamental and Applied Bioenergetics, University Joseph Fourier, BP 53, F-38041 Grenoble Cedex 9, France, E-mail: uwe.schlattner@ujf-grenoble.fr, or Uwe Riek, Institute of Cell Biology, HPM D23.3, Schafmattstrasse 18, ETH Zurich, 8093 Zurich, Switzerland, E-mail: publications@riek.ch.

Heterotrimeric AMP-activated protein kinase (AMPK) is crucial for cellular energy homeostasis of eukaryotic cells and organisms. Recently, we developed a bacterial co-expression strategy for functionally intact full-length mammalian AMPK with a His-tag. Here we report on (i) the bacterial expression of untagged mammalian AMPK isoform combinations, all containing γ_1, (ii) a fully automated 4-dimensional purification protocol, and (iii) a detailed biophysical characterization of AMPK heterotrimers by small angle X-ray scattering in solution (SAXS), transmission and scanning transmission electron microscopy (TEM, STEM) and mass spectrometry (MS). AMPK in solution at low concentrations (< ~1 mg/ml) largely consisted of individual heterotrimers in TEM analysis, revealed a precise 1:1:1 stoichiometry of the three-subunits in MS, and behaved as ideal solution in SAXS. At higher AMPK concentrations, SAXS revealed concentration-dependent, reversible dimerization of AMPK heterotrimers and formation of higher oligomers, also confirmed by STEM mass measurements. Single particle reconstruction and averaging by SAXS and TEM, respectively, showed a similar molecular shape of AMPK heterotrimers revealing elongated, flat particles with protrusions and indentations. In the lower AMPK concentration range, addition of AMP resulted in a significant decrease of the radius of gyration by ~5% in SAXS, which indicates a conformational switch in AMPK induced by ligand binding. Based on our findings we propose a structural model involving a ligand-induced relative movement of the kinase domain resulting in a more compact heterotrimer and a conformational change in the kinase domain that protects AMPK from dephosphorylation of T172, thus positively affecting AMPK activity.

AMP-activated protein kinase (AMPK) and its orthologs found in yeast, plants, insects, invertebrates and vertebrates are fuel sensors of the eukaryotic cell and function as master regulators of energy metabolism (1-5). AMPK is a serine/threonine protein kinase, consisting of one catalytic α and two regulatory-subunits (β and γ), existing as multiple isoforms (α_1, α_2, β_1, β_2, γ_1, γ_2, γ_3) and splice variants (of γ_2 and γ_3), thus allowing for the generation of multiple heterotrimeric isoform combinations. Critical for activation of AMPK is its phosphorylation at T172 in the kinase domain of the α-subunit by either of the two upstream kinases of AMPK, LKB1-MO25α-STRADα or Ca^{2+}/Calmodulin-dependent protein kinase kinase β (CaMKKβ) (6-10). In addition, AMP allosterically stimulates AMPK (10,11) by binding to two pairs of CBS domains in the γ-subunits, called Bateman-domains (12). These domains were reported to show high affinity for AMP (10,13) and lower affinity for ATP (12), although a recent study indicates that affinities may be similar (14). AMP is a very sensitive signal for an altered

cellular energy status (13,15,16). Its intracellular concentration changes by one order of magnitude upon a 1% change in the cellular ATP concentration, due to the equilibrium reaction of adenylate kinase and creatine kinase. The latter uses phosphocreatine to rapidly rephosphorylate ADP to ATP and thus maintains a high ATP/ADP ratio (15-18). Allosteric stimulation of AMPK by AMP increases phosphorylation at T172 and simultaneously inhibits dephosphorylation of this site by protein phosphatase 2Cα, thus decreasing the rate of AMPK inactivation (10,19). The precise function of the AMPK β-subunit is not entirely clear. It contains α and γ interaction domains (20,21), a glycogen binding domain (22,23), and β_1 additionally has an N-terminal myristoylation site that may target AMPK to membranes (24). More recently, an autophosphorylation site at S108 has been involved in the AMP-dependent activation mechanism of AMPK (19).

Cellular energy stress and other signals activate AMPK by various pathways, leading as a main consequence to compensatory measures that increase ATP generation and decrease ATP consumption. However, the AMPK signaling pathway has not only been implicated in cellular energy homeostasis (13,25), but also in the regulation of whole body energy balance (2,26,27), and more recently in energy-dependent regulation of cell shape (4) and cancer signaling (28-32). The latter is mainly due to the tumor suppressor properties of the upstream kinase LKB1 (6,8) and the downstream link to signaling by the mammalian target of rapamycine (mTOR) which is involved in proliferation control (33). Mutations in the AMPK γ-subunit cause several pathologies, mainly due to accumulation of cellular glycogen (34-36). Its multiple downstream effects, including lowering of blood glucose levels, have identified AMPK as a promising target to treat type II diabetes mellitus and the metabolic syndrome (37).

More detailed structural information about mammalian heterotrimeric AMPK is needed to understand its complex molecular architecture and function. Valuable but limited insight has been provided by X-ray structures of isolated AMPK domains: the catalytic domain of the human α_2-subunit (Littler et al., Structural Genomics Consortium, PDB:2H6D) and its yeast ortholog Snf1 (38,39), the glycogen binding domain of the rat β-subunit (40), the Bateman domain of the γ-subunit yeast ortholog Snf4 (41), and a CBS_{3-4}-domain pair of the human γ-subunit (42). More informative, but still limited in their explanatory power, are the recent X-ray structures of truncated versions of a mammalian AMPK complex (14) and its yeast orthologs of *S. pombe* (43) and *S. cerevisiae* (44) (suppl. Fig. 1). For successful crystallization, large truncations were introduced into the mammalian α- and β-subunits or their yeast homologs. The published core structures all lack the α-subunit kinase domain and a more or less large N-terminal part of the β-subunit. In the *S. pombe* and mammalian structures, almost 50% of the entire complex is missing. The *S. cerevisiae* structure (suppl. Fig. 1) is somewhat less truncated and contains a regulatory sequence (RS, α-subunit) and the glycogen-binding domain bound to β-cyclodextrin (β-subunit).

A major contribution of these structures is the exact definition of subunit interactions. They confirm the structural consensus model of AMPK that had been challenged before (20,21). In addition, the larger *S. cerevisiae* structure reveals novel interactions of the γ-subunit homologue with both the regulatory domain (α-subunit) and the glycogen binding domain (β-subunit). The structures also identify the precise nucleotide binding sites on the γ-subunit (see also Fig. 9B). While in yeast only a single AMP (or ATP) molecule is bound to the γ-homolog (43,44), probably because yeast AMPK is not activated by AMP, the mammalian AMPK γ-subunit revealed three nucleotide binding sites (14). One site, corresponding to the yeast binding site, contains a non-exchangeable, fixed AMP, while the other two allow for ATP/AMP exchange and thus provide the AMP sensor function of AMPK. However, neither of the AMP-containing AMPK core structures showed an appreciable structural difference as compared to ATP-containing or nucleotide-free structures. This observation and the absence of the kinase domain in all known AMPK core structures have so far hampered a molecular explanation for AMP-dependent activation of the holo-complex. This mechanism necessarily involves a cross talk between AMP binding on γ and the activating T172 phosphorylation on the α kinase domain, which most likely implies a conformational change and/or a domain movement. Thus, although extremely valuable, the known structures are unable to explain the functioning of the entire holo-complex. Detailed analysis the full-length mammalian AMPK heterotrimer and its dynamic structure upon activation is obviously necessary.

Here we report on the molecular shape of γ_1-containing AMPK holoenzyme-complexes obtained using different biophysical approaches. We have set up a high level expression and automated purification protocol of untagged protein on the basis of our His_6-tagged tricistronic expression system (45). It yields sufficient quantities of homogeneous functional kinase complexes without the need of a potentially interfering purification tag. This allowed us to study AMPK in solution by small angle X-ray scattering (SAXS) and by different electron microscopy (EM) techniques, including single particle reconstruction. These data characterize AMPK as an elongated, flat particle with a large indentation and a protrusion. Importantly, they demonstrate a ligand-induced conformational change of the AMPK heterotrimer upon binding of AMP.

EXPERIMENTAL PROCEDURES

Plasmids and expression of proteins in bacteria – Tricistronic AMPK expression plasmids were constructed as described earlier (45), but encoding non-tagged versions of the four different mammalian AMPK isoform combinations $\alpha_1\beta_1\gamma_1$, $\alpha_2\beta_1\gamma_1$, $\alpha_1\beta_2\gamma_1$, and $\alpha_2\beta_2\gamma_1$ (Genbank Acc. No. U40819, Z29486, X95577, AJ224538, X95578). Proteins were expressed in Tuner (DE3) *E. coli* cells (Novagen, EMD Chemicals Inc., Darmstadt, Germany). Expression of AMPK in rich medium in a self-constructed fermenter will be described elsewhere (Riek et al., unpublished). Preculturing and expression in minimal medium was developed for full-length heterotrimeric AMPK and was later also successfully applied for the expression of LKB1 complex as described recently (46). The same method was used here for AMPK expression in a 42 liter bioreactor (MBR Switzerland), except that the growth temperature was kept at 34°C, or in a 5 liter bioreactor (Minifors, Infors AG, Switzerland), except for some adaptations to the reduced vessel volume. After inoculation with cells from 400 ml pre-culture, batch growth was continued for 12 h overnight at 32°C, with a stirrer speed at 1000 rpm and an air flow of about 4 l/min until depletion of glucose and acetate (pO_2 ~100%). The feed was balanced with O_2 consumption until reaching pO_2 limitation at the maximal air flow (~7-8 l/min; to obtain such high air flow, the original air inlet filter was changed to an AcroPac 300, Pall, Switzerland) at maximal stirrer speed (1250 rpm). Protein expression was induced with 50 mg/l iso-propylthio-β-D-galactopyranoside (IPTG) at around OD_{600nm} = 25 for 7.5 h at 34°C.

Bacteria were harvested by centrifugation, washed in physiological NaCl solution and immediately frozen in liquid nitrogen. The yield per fermentation, expressed as wet weight bacterial pellet, was reproducibly 200-250 g or 1200-1400 g in the 5 l or 42 l bioreactor with 3 or 27 l medium, respectively.

Protein extraction – A 70 g aliquot of the frozen bacterial pellet was resuspended in lysis buffer (LysB: 30%(w/v) glycerol, 0.5 M sucrose, 50 mM HEPES, 2 mM $MgCl_2$ pH 8.0 at 7°C) to a total volume of about 200 ml. Cells were lysed with an Emulsiflex C5 high pressure homogeniser (Avestin, Germany), first applying 100-300 bar to resuspend cells, and then using 1200-1500 bar for cell lysis. The lysate was supplemented with 7 µl Benzonase (purity grade II, Merck, Germany), stirred gently at 4°C for 1h, and centrifuged at 23,000 g for 1 h to pellet cell debris. The clear supernatant was used for HPLC purification.

Protein purification – A new protocol was developed based on (i) the fact that untagged AMPK heterotrimer is able to bind to some metal affinity matrices, and on the availability of (ii) an Äkta Explorer 100 Air HPLC system (GE Healthcare, Otelfingen, Switzerland) that was modified to allow automated multi-dimensional purification. Details of the machine setup will be published elsewhere (Riek et al., unpublished). The setup used here included following columns: (i) XK 26/40 (GE Healthcare, Switzerland) containing 140 ml Protino Ni-IDA (Macherey Nagel, Switzerland), (ii) XK 26/20 containing 45 ml with Reactive Red 120 fast flow highly cross-linked 6% Agarose (R-6143 Sigma, Switzerland), (iii) two 1 ml Ni-HP columns (GE Healthcare), (iv) Superdex 200 16/60 (GE Healthcare); as well as a 10 ml Super-loop (SL) (GE Healthcare) at the first injection valve. The buffers used were: elution buffer (EluB: as LysB, but with the addition of 250 mM Imidazol), Red Sepharose elution buffer (RSEluB: as LysB, but with the addition of 600 mM NaCl), Ni-HP elution buffer (HPEluB: as EluB but with the addition of 200mM NaCl and 2 mM Tris(2-carboxyethyl)phoshine hydrochloride (TCEP), size exclusion buffer one (SE1: 200 mM NaCl, 50 mM HEPES, 10 mM $MgCl_2$, 8 mM EDTA, 2 mM TCEP pH 8.0 at 7°C), size exclusion buffer two (SE2: as SE1, but without EDTA and with only 2 mM $MgCl_2$).

The fully automated purification procedure was carried out at 7°C except for the Superdex column, which was run at 25°C. Sample tubing at S1, S2, and S3 were connected to vessels containing LysB, EluB and RSEluB, respectively, and were primed manually. The Ni-IDA column was equilibrated with LysB, the Reactive Red column with EluB, and the Ni-HP column with RSEluB. Tubing and valves were flushed with the appropriate buffers. Bacterial lysate was added to the sample vessel S1 and the automated run was started. Lysate was then applied to the Ni-IDA column at a flow rate of 4 ml/min using an air sensor to stop direct load injection. The column was washed with 160 ml LysB (flow rate 5 ml/min at maximal 0.5 MPa pressure feedback). After flushing the system and P960 with EluB, elution was done with EluB (5 ml/min, max. 0.5 MPa). Elution fractions between 63 and 156 ml after EluB application were recovered in the S2 vessel and re-injected into the Reactive Red column at a flow rate of 1 ml/min, max. 0.2 MPa. After washing with 94 ml LysB at 2 ml/min (max 0.2 MPa), the volume eluting between 20 and 95 ml after application of RSEluB, was collected in the S3 vessel and re-injected into the Ni-HP columns (1 ml/min, max. 0.4 MPa). Columns were washed with 8 ml LysB (0.5 ml/min, max. 0.4 MPa) and eluted with EluB. A 5 ml peak fraction (starting at OD_{280}>600 mAU) was collected in the SL. The Superdex column was equilibrated with 200 ml SE1 buffer (1.6 ml/min, max. 0.1 MPa) and, finally, 4 ml of the SL fraction were loaded and 1 ml fractions were collected. Material left in the tubing and SL was collected later in separate fractions.

For MS, STEM, TEM, SAXS, crystallization and activity experiments, the first part of the size exclusion peak showing the highest specific AMPK activity was pooled, and subjected to a second size exclusion chromatography on the same Superdex column but using SE2 buffer without EDTA. Protein concentrations were determined according to Bradford (47) using Bio-Rad microassay (Biorad, Reinach, Switzerland) in SE2 buffer, calibrated by the 280 nm extinction coefficient for unfolded AMPK protein ($\alpha_1\beta_1\gamma_1$: 0.911 and $\alpha_2\beta_2\gamma_1$: 0.892 g/l).

Dynamic light scattering – The dynamic light scattering (DLS) signal was recorded on a DynaPro molecular-sizing instrument (Protein Solutions, now Wyatt). Samples after elution from the second size exclusion chromatography were concentrated to 10 mg/ml in SE2 buffer and centrifuged at 4°C and 20,000 g for 30 min prior to the measurements. Data were acquired using a 50 µl sample in an Eppendorf UVette cuvette at 20°C with 10 s acquisition intervals and maximum laser intensity and analyzed with the software Dynamics.

Enzyme activity assay – Following full activation by upstream kinases, activity of purified AMPK was determined by phosphorylation of the synthetic substrate SAMS in presence of saturating AMP concentrations, using a non-radioactive, HPLC-based method that quantifies SAMS, phospho-SAMS, AMP, ADP and ATP, as described previously (10).

Scanning Transmission Electron Microscopy (STEM) – Cross-linking of 1 mg/ml AMPK obtained in SE2 buffer after a second size exclusion chromatography was done at a final concentration of 1% glutaraldehyde (Fluka, Switzerland) for 60 s on ice and was quenched with Tris pH 8.0 at 4°C. The cross-linked AMPK was then repurified by size exclusion on column 4 in SE2 to remove aggregates. An aliquot of this preparation was diluted 4× in SE2 buffer, and 5 µl-aliquots were adsorbed for 60 s to glow-discharged STEM films (thin carbon films that span a thick fenestrated carbon layer covering 200-mesh/inch, gold-plated copper grids). The grids were blotted, washed on 5 drops of quartz double-distilled water, and freeze-dried at -80°C and 5×10^{-8} Torr overnight in the microscope. Tobacco mosaic virus (TMV) particles (kindly provided by R. Diaz Avalos, University of California, Davis, USA) were used for absolute mass calibration. These particles were similarly adsorbed to separate STEM films, washed on 4 drops of 10 mM ammonium acetate, and air-dried. A Vacuum Generators STEM HB-5 interfaced to a modular computer system (Tietz Video and Image Processing System GmbH, Gauting, Germany) was employed. Series of 512×512-pixel, dark-field images were recorded from the unstained sample at an acceleration voltage of 80 kV and a nominal magnification of 200,000×. The recording dose ranged from 474 to 945 electrons/nm^2. The digital images were evaluated using the software package IMPSYS (48). Accordingly, the projections were selected in circular boxes, and the total scattering of each region was calculated. The background scattering of the carbon support film was then subtracted, and the mass was calculated. The results were scaled according to the mass measured for TMV and corrected for beam-induced mass loss according to the behavior of proteins in a similar mass range ((49) and

unpublished data). The mass values were then displayed in histograms and described by Gauss curves. The overall experimental uncertainty of the results was estimated from the corresponding SE (SE = SD/√n) and the approximate uncertainty of 5% in the calibration of the instrument. The number of particles giving rise to each peak, n, was estimated by measuring between the points of peak overlap.

To aid peak assignment, galleries were created displaying particles with masses ± 20 kDa from each peak. Average images were calculated using the EMAN program package (50).

Transmission electron microscopy (TEM) and image processing – AMPK samples were diluted (in SE2) to 20 µg/ml. Aliquots of 5 µl were stained with 2% (w/v) uranyl acetate after sample adsorption onto glow discharged 400 mesh carbon-coated grids. The micrographs were recorded at an accelerating voltage of 100 kV and a magnification of 50,000×, using a Hitachi 7000 electron microscope. All micrographs were recorded on Kodak SO-163 film. The electron micrographs were digitized with a Heidelberg Primescan (Germany) scanner at 4 Å/pixel (resolution at the sample level). Manually selected particle projections were subjected to reference-free alignment and classification by multi-variant statistical analysis using the EMAN software package (50). The class averages with the best signal-to-noise ratio were gathered in a gallery.

Mass spectrometry (MS) – The AMPK complex was analyzed after chemical cross-linking performed with a mixture of cross-linkers (CovalX K100 MALDI MS stabilization kit, Zurich, Switzerland). The cross-linking chemistry and specificity has been studied and described (51). 10 µl of AMPK complex at 2 µM was submitted to the cross-linking reactions and incubated on ice for 1 h to achieve complete reaction. After cross-linking, 1 µl of the sample containing the stabilized complex was mixed with 1 µl of the matrix solution of sinapic acid (10 mg/ml) in acetonitrile/deionized water 1:1 (v/v) and 0.1% TFA. After mixing, 1 µl of the mixture was dropped onto the MALDI plate using the dried droplet method.

High-mass MALDI ToF mass spectra were obtained using a Reflex III MALDI ToF mass spectrometer (Bruker Daltonics, Bremen, Germany) equipped with a HM1 high-mass detection system (CovalX, Zurich, Switzerland). The instrument was operated in linear mode by applying and accelerated voltage of 25 kV. Mass spectra were acquired by averaging 200 shots. The laser pulse energy was adjusted slightly above threshold for ion production. The mass spectra were acquired after external calibration with a mixture of 4 proteins covering a 6-150 kDa range. The mass spectrometric data were analyzed using Complex Tracker software (CovalX AG, Zurich, Switzerland). The software allows the overlay and subtraction of control and cross-linked spectrum for characterization of intact protein complexes analyzed by High-Mass MALDI ToF mass spectrometry.

Small angle X-ray scattering in solution (SAXS) –The synchrotron SAXS data were collected at DESY (Hamburg, Germany) on the X33 camera of the EMBL (52,53). Two isoforms of wild type AMPK ($\alpha_1\beta_1\gamma_1$ and $\alpha_2\beta_2\gamma_1$) in SE2 with and without 1 mM AMP were analyzed at protein concentrations ranging from 0.5 to 18 mg/ml. Data were recorded using a MAR345 image plate detector at a sample-detector distance of 2.4 m and a wavelength $\lambda = 0.15$ nm, covering the range of momentum transfer $0.12 < s < 4.5$ nm^{-1}. No radiation damage was observed during two 2-minute test exposures. The data were reduced, processed and the overall parameters were computed following standard procedures of the software package PRIMUS (54,55).

The forward scattering I(0) and the radius of gyration R_g were evaluated using the Guinier approximation (56) assuming that at very small angles ($s < 1.3/R_g$) the intensity is represented by $I(s) = I(0) \exp(-1/3(sR_g)^2)$. These parameters were also computed from the entire scattering patterns using the program GNOM (57), also yielding the maximum particle dimension D_{max}. The molecular masses (MM) of the solutes were evaluated by comparing the forward scattering with that of reference solutions with bovine serum albumin. The excluded volume of the hydrated particle (Porod volume *V* (58)) was computed using the equation (1):

$$V = 2\pi^2 I(0) / \int_0^\infty s^2 I_{\exp}(s) ds \qquad (1)$$

(I_{exp} experimental data as function of momentum transfer *s*)

Prior to this analysis, an appropriate constant was subtracted from each data point to force the s^{-4} decay of the intensity at higher angles following Porod's law for homogeneous particles. This "shape scattering" curve was further employed to generate low resolution *ab initio* models of monomeric AMPK

heterotrimers using the program DAMMIN (59), which represents the protein by an assembly of densely packed beads. Simulated annealing (SA) is employed to build a compact interconnected configuration of beads inside a sphere with the diameter D_{max} that fits the experimental data $I_{exp}(s)$ to minimize discrepancy:

$$\chi^2 = \frac{1}{N-1}\sum_j \left[\frac{I_{\exp}(s_j) - cI_{calc}(s_j)}{\sigma(s_j)}\right]^2 \quad (2)$$

where N is the number of experimental points, c is a scaling factor and $I_{calc}(s_j)$ and $\sigma(s_j)$ are the calculated intensity and the experimental error at the momentum transfer s_j, respectively. The results from ten runs for each type were averaged using the program DAMAVER (60), which superimposed the models pairwise to generate the most typical model by retaining the common structural features.

RESULTS

Purification – The presence of a purification tag in a recombinant protein may cause problems for its biophysical or biochemical characterization, especially for crystallization. Attempts to remove the His-tag from tagged AMPK after purification were unsuccessful, partly due to precipitation of AMPK after cleavage and protein loss during IMAC employed to remove uncleaved AMPK. Further analysis revealed that untagged AMPK also bound to the IMAC column (data not shown). Based on this finding, a 4-dimensional purification protocol was developed on a highly modified commercial HPLC (Riek et al., unpublished). It applies first IMAC, second a nucleotide analog affinity chromatography (Reactive Red 120 agarose), third another IMAC for sample concentration and fourth a preparative size exclusion column. This procedure was automated and optimized for minimum total runtime (~18.5 h, suppl. Fig. 2A), convenience and reproducibility, rather than maximum yield (about 10-15 mg AMPK per 70 g wet weight bacterial pellet). Several-subunit isoform combinations ($\alpha_1\beta_1\gamma_1$, $\alpha_2\beta_1\gamma_1$, $\alpha_1\beta_2\gamma_1$, and $\alpha_2\beta_2\gamma_1$) were bacterially expressed and purified according to this protocol. AMPK eluted from the final calibrated gel filtration column at an elution volume corresponding to ~240 kDa. This is a higher MM than expected for heterotrimers, indicating a strong non-sphericity of these particles. Coomassie-Blue stained SDS-PAGE gels of the peak fractions revealed the general homogeneity of the preparations with three distinct protein bands at the expected molecular weight corresponding to the α-, β-, and γ-subunits of AMPK (Fig. 1A).

A final, second size exclusion chromatography run was performed to remove EDTA, which was included in the buffer of the first size exclusion chromatography to chelate Ni^{2+}-ions leaking from the preceding IMAC column. Functional integrity of these final AMPK preparations was verified by activity determination using CaMKKβ for activation and AMP for maximal stimulation. Maximal specific activities of the elution fractions were further increased compared to the first size exclusion step, changing from ~4 to ~6 μmol phospho-SAMS $min^{-1}mg^{-1}$ (suppl. Fig. 2B), which is comparable to those reported earlier (10). However, it should be noted that specific kinase activity was always slightly higher in the first half of the size exclusion peak.

Taken together, the new automated protein purification scheme resulted in highly purified and enzymatically functional untagged full-length AMPK. Either such untagged protein or the earlier His_6-tagged version (45) have been successfully used in several studies (10,19,61-68).

Dynamic light scattering – $\alpha_1\beta_1\gamma_1$- and $\alpha_2\beta_2\gamma_1$-AMPK samples concentrated to 10 mg/ml showed a polydispersity of about 20% and a hydrodynamic radius of about 5.6-7.5 nm in dynamic light scattering (Fig. 1B). This results in a calculated MM range of 210-380 kDa. Since the expected MM of the αβγ AMPK heterotrimers is roughly 130 kDa, this data suggests the formation of dimers or higher oligomers at elevated concentration.

Scanning Transmission Electron Microscopy – For mass determination by STEM, a solution of $\alpha_2\beta_2\gamma_1$ AMPK at 1 mg/ml was reacted with 1% glutaraldehyde to conserve the native complexes prior to the dilutions required for microscopy. The cross-linking efficiency was verified by SDS-PAGE and any large unspecific oligomers were removed by size exclusion chromatography as described above. The unstained AMPK particles were imaged by STEM (Fig. 2A), manually sorted according to their dimensions (small, medium, large), and subsequently analyzed for their mass as shown in the three histograms (Fig. 2B-D). The major particle population (Fig. 2B,C) mainly contained single heterotrimers (expected MM ~130 kDa) including the peaks at 142 (±33) kDa (n~766; arrow in Fig. 2B) and 130 (±21) kDa (n~124; arrow in Fig. 2C). These two peaks arise from

particles of different size (~11 x 8 nm and ~8 x 7 nm in diameter; estimated uncertainty in longest dimension ±1nm), which may be interpreted as side and top views of the heterotrimer. A minor particle population (Fig. 2D) showed a peak at 296 (±28) kDa (n~73; arrow in Fig. 2D), indicating the additional presence of dimers of these heterotrimers as already seen by dynamic light scattering experiments in more concentrated solutions. The minor histogram peak at 83 (± 21) kDa (n~36; Fig. 2C) is not significant and may be assigned to a small number of dissociation products, while the peaks at 221 and 392 (±28) kDa (n~52 and ~17, respectively; Fig. 2D) relate to some unspecific association. The existence of AMPK heterotrimers and dimers thereof was corroborated by the prior SDS-PAGE separations of cross-linked AMPK material (not shown).

High-mass MALDI ToF MS – To analyze the composition of AMPK complexes, the $\alpha_2\beta_2\gamma_1$ AMPK was subjected to high-mass MALDI ToF MS. Without chemical cross-linking, three different polypeptides were detected in the overlay spectrum (Fig. 3A, black trace: m/z=62.26, 30.24 and 37.38 kDa;). They very precisely correspond to the expected MM of the three individual-subunits α_2 (62.32 kDa), β_2 (30.23 kDa) and γ_1 (37.58 kDa). To distinguish between $\alpha_2\beta_2\gamma_1$ heterotrimers (130.13 kDa) and a possible $(\beta_2\gamma_1)_2$ complex of similar size (135.56 kDa), MS of the entire cross-linked AMPK complexes was conducted (Fig. 3A, red trace). Intact complex was clearly detected with m/z=129.95 kDa, corresponding to the $\alpha_2\beta_2\gamma_1$ heterotrimer. The subtraction spectrum (Fig. 3B) confirmed the presence of the heterotrimer ion $[\alpha_2\beta_2\gamma_1]^{+1}$, together with a peak at m/z=64.97 kDa representing the doubly charged heterotrimer $[\alpha_2\beta_2\gamma_1]^{+2}$. These data confirm the correct heterotrimeric stoichiometry and the absence of $(\beta\gamma)_2$ complexes.

Transmission electron microscopy – TEM of negatively stained $\alpha_2\beta_2\gamma_1$ AMPK revealed a major population of elongated particles with a maximum length of approximately 11 nm (± 1nm, Fig. 4). Comparison with the dimensions of the ~130-140 kDa particles analyzed by STEM, allowed their assignment as heterotrimers. Reference-free alignment and classification of 937 such particles yielded class averages corresponding to different orientations of the molecules on the carbon film. The molecules appear elongated and show some cavities giving them a "cashew nut"-like appearance.

Small angle X-ray scattering – Particle characterization in solution with SAXS was applied to wild type AMPK of the two-subunit isoform combinations $\alpha_1\beta_1\gamma_1$, and $\alpha_2\beta_2\gamma_1$. The experimental SAXS curves for different protein concentrations are shown in Figures 5 and 6, the corresponding integral structural data are presented in Table 1.

First of all, the data show that the size of the scattering particle depends on protein concentration. At high AMPK concentrations generally used for SAXS, an oligomerization of AMPK occurred (Fig. 6, Table 1). AMPK concentrated to 10-20 mg/ml occasionally showed some unspecific large aggregates, but mostly specific, larger but homogeneous particles (D_{max} ~25-30 nm) in the size range of AMPK heterotrimer dimers. Upon dilution of such concentrated AMPK solutions, a decrease of the R_g and D_{max} was observed, leading to values similar to those observed for samples that had always remained at low protein concentration. Therefore, the observed dimerization of AMPK heterotrimers is a reversible, concentration dependent process. Upon decreasing AMPK concentration further below ~1 mg/ml (Fig. 5A, Table 1), the scattering signal became concentration-independent and no further decrease of maximum size and radius of gyration of AMPK particles occurred for both, $\alpha_1\beta_1\gamma_1$- and $\alpha_2\beta_2\gamma_1$-AMPK. Such ideal, monodisperse solutions (in SAXS terms) were represented by a homogeneous population of monomers of AMPK heterotrimers with a maximum particle dimension D_{max} of 16 ±1 nm, a maximum of the distance distribution function of ~5 nm and a MM of roughly 140 kDa. The larger dimensions and additional mass of heterotrimers compared to calculated data and to those determined in TEM/STEM can be explained by the presence of the hydration shell and the potential flexibility of the AMPK complex (69), both of which increase the size seen by SAXS. Further, in the case of EM, an influence of adsorption on the flexible AMPK heterotrimer cannot be entirely ruled out; interaction with the carbon film of the grid might favor more compact conformations of the complex.

The latter ideal AMPK solution, i.e. a protein concentration below ~1 mg/ml, is a precondition to study the binding of the ligand AMP, or to model the heterotrimeric AMPK particle from SAXS data. Addition of the allosteric activator AMP induced a noticeable change in the AMPK scattering curves (Fig. 5B)

and in the derived radii of gyration (R_g, Table 1), while the maximum particle dimension (D_{max}, Table 1) remained constant. This clearly indicates that AMP-binding leads to more compact particles (Fig. 6A). At higher, non monodisperse protein concentrations, addition of AMP also decreased R_g (not shown). However, these results are ambiguous, since it is impossible to distinguish between effects caused by changes in the dimerization equilibrium induced upon ligand binding and changes in the shape of the scattering particles themselves.

Models of the molecular shape of monodisperse heterotrimeric $\alpha_1\beta_1\gamma_1$- and $\alpha_2\beta_2\gamma_1$-AMPK in solution were calculated using the DAMMIN software in the "keep" mode and assuming P1 symmetry (no symmetry). Individual molecules were represented by elongated, curved particles showing a deep indentation and a protrusion (Fig. 7). Some of these features are less evident in averaged and filtered models based on 10 different, individual models each calculated from data obtained without (Fig. 8 green) or with AMP added (Fig. 8 red). Arithmetic averages of the radii of gyration and the excluded model volumes calculated from these models by DAMMIN again showed a consistent and significant change of about 5% towards a more compact scattering particle upon AMP ligand binding.

DISCUSSION

This study provides a first detailed structural characterization of untagged, full-length heterotrimeric AMPK by applying a variety of independent but complementary biochemical and biophysical analytical tools. The quantitative results obtained suggest that AMPK heterotrimers are not spherical but rather elongated, curved particles that have a strong tendency to dimerize. Most importantly, allosteric activation by AMP is shown to involve a conformational change towards a more compact heterotrimer.

Large quantities of untagged, native AMPK are essential for biophysical analysis – High yield bacterial expression and the novel purification protocol for untagged AMPK were instrumental for this study, providing the large amounts of purified, native protein required for biophysical characterization, especially for SAXS or isothermal titration calorimetry (ITC). Implementation of the automated 4-dimensional purification procedure aimed at increased reproducibility and minimal process time without reducing the purity of the final preparation. This could be achieved by the use of frozen bacterial pellet aliquots from fermentation single runs and the setup of a user-modified Äkta Explorer™ (Riek, et al., unpublished). The latter provided reproducible instrumental precision, reduced the time needed for purification to about 18.5 h overnight (as compared to one week with manual operation), and gave a final overall yield of about 10-15 mg AMPK per 70 g wet weight bacterial pellet. Availability of freshly purified AMPK was in particular essential for methods that require large amounts of material and/or that are incompatible with glycerol, like SAXS, STEM, TEM or ITC. Otherwise, addition of 50% glycerol is necessary to stabilize AMPK for longer time periods (10). Such purified AMPK could be activated by CaMKKβ and further stimulated by the allosteric activator AMP, reaching a rather high specific activity of 6 µmol phospho-SAMS $min^{-1}mg^{-1}$. In a previous study using this protein (10), we could show that AMP does not affect AMPK phosphorylation by the upstream kinases LKB1/MO25α/STRADα or CaMKKβ (6-9), but inhibits AMPK dephosphorylation by PP2Cα (10). It was also shown that the combined activation effects are more than 1000-fold, thus much larger than thought previously (10). These data corroborate the functional integrity of the native AMPK preparations with respect to activation and deactivation mechanisms. To distinguish between the αβγ heterotrimers and possible (βγ) dimers with very similar MM, MS of the entire cross-linked AMPK complexes was conducted. The data revealed a correct heterotrimeric stoichiometry and the absence of $(\beta\gamma)_2$ contamination.

Reversible dimerization of AMPK at higher protein concentrations – High concentrations of protein (above 10 mg/ml) are generally used for in solution characterization of protein structures by SAXS to obtain an optimal signal to noise ratio. Under these conditions, the data revealed a strong tendency of AMPK heterotrimers to form dimers. In addition, first results with SAXS and DLS (not shown) indicated a concentration dependent occurrence of further higher oligomers of the heterotrimer, as well as some unspecific aggregates or precipitates, especially upon exposition of the protein to stronger shearing forces by inappropriate handling, e.g. careless pipeting. This indicates a tendency of AMPK to form higher aggregates or to even denature *in vitro*, as

also noted during the development of the AMPK purification protocol. However, if handled with sufficient care, AMPK did not just aggregate, but rather formed dimers of native heterotrimers. This was confirmed independently by electron microscopy methods, being single molecule rather than bulk techniques. Dimers of AMPK heterotrimers were detected in small amounts by TEM, and also by STEM, the latter allowing exact mass measurements of oligomers after the chemical cross-linking.

As shown in further SAXS experiments, the dimerization process is a concentration-dependent and reversible process. Dilution of concentrated AMPK solutions led to a decrease in particle size, until values comparable to those from AMPK samples that had been purified and maintained at such low protein concentrations. Samples diluted immediately (~1 min) before starting the 2 min X-ray exposure for SAXS were no different to undiluted low concentration samples or samples examined a longer time after dilution. Therefore, the timescale for the reversible concentration-dependent dimerization equilibrium must be much less than 3 min.

Dimerization may in fact be an intrinsic, conserved property of the AMPK kinase family and even physiologically relevant. The catalytic domain of SNF1, the yeast ortholog of AMPK, not only forms crystallographic dimers by a conserved and accessible surface motif, but also dimerizes in solution (38,39,70). Mammalian AMPK is not an abundant cellular protein, but different mechanisms may lead to higher local AMPK concentrations than commonly anticipated. These include compartmentation at defined subcellular loci (24,71), e.g. in the cell nucleus or at biological membranes via the myristoyl anchor, and molecular crowding effects. Thus it may be entirely reasonable to speculate that dimerization of AMPK could occur at such defined subcellular loci. However, for dimerization of AMPK to occur *in vivo*, not only AMPK concentration is important, but also the concentration of water in the cytosol and its activity coefficient(s) have to be considered.

AMP-binding to AMPK induces a conformational change – Dilution of AMPK samples below 1 mg/ml did not result in a further decrease of particle size in SAXS, indicating that a thermodynamically ideal, mono-disperse protein solution had been reached. This is an absolute prerequisite for the interpretation of SAXS data when analyzing ligand effects or for single particle modeling (see below). In such mono-disperse AMPK solutions, binding of the allosteric activator AMP induced a clear and significant change in the particle conformation as directly seen by SAXS. The radii of gyration of both AMPK isoforms examined were reduced by about 5%, while the maximum particle dimensions remained constant. Comparative averaged SAXS models of AMPK with and without AMP (Fig. 8) indicate that the conformational change induced by ligand binding is likely to be a more radial movement of MM, involving a domain movement tangentially along the long axis of the molecule, rather than an axially oriented shift of MM. Such a change, together with the observed decrease of MM by extrapolation to I(0), as well as the decrease of both the Porod volume and the excluded DAMMIN-model volume, would be consistent with a cleft-closing model in the AMPK heterotrimer upon binding of AMP due to loss of hydration shell water.

ITC was applied in an attempt to directly measure AMP binding constants to AMPK. However, even modern, state of the art microcalorimeters require AMPK concentrations significantly above 1.5 mg/ml to generate a signal that would allow analysis of the potentially three independent AMP binding sites (two Bateman domains, one kinase domain). However, as shown by SAXS, in this concentration range the dynamic, concentration-dependent dimerization equilibrium of AMPK heterotrimers is probably influenced by AMP binding, adding a further energy parameter to the system and, thus, making ITC intrinsically unsuitable for the determination of the exact ligand binding constants for AMPK. So far, K_D values for AMP have been only determined for the Bateman domains in the isolated γ-subunits or the truncated mammalian core complex, ranging from 20 to 125 μM (12,14). Thus, with the AMP concentration of 1 mM used in our study, we clearly saturated the AMP binding sites.

AMPK heterotrimers are elongated, curved particles – In solution SAXS and single particle TEM were applied as complementary techniques to analyze molecular dimensions and shape of AMPK complexes. When using SAXS and procedures for particle reconstruction like DAMMIN, any deviation of an ideal solution has to be strictly avoided. Although heterotrimeric full-length AMPK can exist as monomers and dimers, the equilibrium between both is concentration-dependent. A monodisperse solution (in SAXS terms) of monomers-of trimers was obtained at protein concentrations

below 1 mg/ml (Table 1). However, this reduced the signal-to-noise ratio of SAXS measurements.

The STEM analysis provided a first estimate of both the mass and particle dimensions of the heterotrimers. This guideline ensured that the projections later selected from the negative stain TEM images and averaged (Fig. 5) indeed arose from heterotrimers.

Some differences in particle dimensions between SAXS and single particle TEM were observed. The maximum distance D_{max} inside the scattering AMPK particle, obtained by the distance distribution functions in SAXS, was 16 ±1 nm, while particle with a size of 11 ± 1 nm were obtained by TEM with negatively stained AMPK and by STEM with cross-linked AMPK, respectively. Such differences may be largely due to the hydration shell and the rapid molecular dynamics of flexible AMPK molecules observed with the SAXS in-solution method (69). In addition, it cannot be excluded that more compact conformations were favored on adsorption to the EM grid adding to the size discrepancy.

Despite these explainable differences, the molecular shape of the SAXS models calculated by DAMMIN and the averaged pictures obtained by single particle TEM look strikingly similar. Both reveal large particles with an elongated, curved structure and a wider and a narrower end. This overall shape and appearance resembles that of a cashew nut. The SAXS models show an additional protrusion emanating perpendicularly from the more planar particle, as well as a deeper indentation. The latter feature is not seen in the TEM pictures, possibly due to a preferred orientation of the particles on the carbon film of the EM grid. Interestingly, the recent X-ray structure of the AMPK core complex of the S. *cerevisiae* AMPK homologue, SNF1, which contained most of the β-subunit, showed that the latter protruded perpendicularly to the long axis of the molecule (44). Thus, the protrusion resolved here by SAXS might either represent the kinase domain of the α-subunit or the β-subunit. However, the large truncations in the published high resolution X-ray structures (43,44) preclude precise fitting of these data into the low resolution SAXS model.

The presence or absence of AMP also changed the appearance of the DAMMIN models of AMPK. Without AMP, the complex appeared very elongated with some protrusions exposed, while AMP binding changed the molecule to a more compact shape preferentially at one end of the particle (compare Fig. 8A,B). Since the heterotrimeric core of AMPK does not change conformation upon binding of AMP (14), the conformational change observed here by SAXS must have its structural basis in other parts of the molecule, i.e. in the α-subunit, which contains the kinase domain, or in the β-subunit, which contains the glycogen-binding domain. The conformational change upon AMP binding would thus be consistent with a relative movement of the α- and/or β-subunit, or domains thereof, along the long-axis of the molecule towards the γ-subunit. This would lead to a change in mass distribution and thus to a more compact molecule. The fact that the regulatory domain of the α-subunit was shown to interact tightly with the γ-subunit in the *S. cerevisiae* SNF1 structure (44) would favor such an interpretation.

Full-length AMPK reveals properties different to AMPK core complexes – The most recent X-ray structures of severely truncated core complexes of mammalian AMPK (14) and its orthologs in *S. pombe* (43) and *S. cerevisiae* (44) reveal two structural properties that are relevant to our study: (i) the yeast enzymes occur as crystallographic dimers-of-trimers, and (ii) no major conformational differences are observed between the apo-enzyme and the AMP- (or ATP)-bound state.

Tight dimers of yeast AMPK orthologs seem to occur readily in crystals (39,43,44), but also in solution (39). However, dimerization occurs at various different interfaces: between α- and γ-subunits in the *S. pombe* core complex (43) (whether this interface is accessible in the full-length holoenzyme remains an open question), between γ-subunits in the *S. cerevisiae* core complex (44), and between the kinase domains with individual Snf1 α-subunit orthologs (39). These latter interactions could also occur in full-length heterotrimeric AMPK complex, but the mechanism of dimer formation in solution and its putative role *in vivo* await future clarification.

Significant conformational changes upon binding of AMP or ATP were neither observed in the *S. pombe* complex (43), nor in the truncated mammalian AMPK (14). This may simply be due to the large truncations (Fig. 9), in particular to the absence of both the autoinhibitory and kinase domains (43). However, it is also unknown whether the yeast complexes are activated by AMP at all, thus precluding definite conclusions on the activatory mechanism of mammalian AMPK. AMP binding to Bateman domains in the γ-subunit of

mammalian AMPK leads to activation of the kinase domain in α, suggesting a cross-talk between these two-subunits. The conformational change observed with full-length, native AMPK in our study provides a possible mechanism for this cross-talk.

A model for AMPK activation – Combining X-ray structural information (14,43,44) with known biochemical and biophysical data on the regulation of AMPK (10,11) and the observed conformational change upon AMP binding (this work), we propose a new structural model for AMPK. The model is based on the AMPK ortholog of *S. cerevisiae* (Fig. 9A, PBD:2QLV, Ref. (44)). Since only one AMP moiety was partially resolved (as in the *S. pombe* structure), the three AMP molecules observed in the mammalian AMPK core complex (14) were fitted into the homologous yeast sites by superposition. Turning the representation as published in Amodeo et al. (Fig. 9B and suppl. Fig. 1) by 90°, it is obvious that one exchangeable AMP-binding site (site 1) in the γ-subunit (Fig. 9B, *blue*) is very close to the regulatory sequence of the α-subunit (RS, Fig. 9B, *red*). The second AMP-binding site (site 2) and the site containing a non-exchangeable, fixed AMP (site 3) are somewhat more distant to the RS. Further, the X-ray structure of the isolated AMPK kinase domain (Littler et al. 2006, Structural Genomics Consortium; PDB:2H6D) was positioned with the active site pointing to the outside of the complex (Fig. 9B, *grey*). From this topology it is obvious that the RS together with a neighboring sequence, which are missing in the crystallized structures (including a putative regulatory helix suggested by Pang and colleagues (72)), are sandwiched in-between the γ-subunit and the α-subunit kinase domain. It is thus entirely conceivable that a small conformational change and/or a change in the γ-subunit surface charge upon AMP binding (as in the *S. pombe* X-ray structure, see Figs 2D,F in (43)) could be transmitted via the RS onto the kinase domain and possibly other domains of AMPK (Fig. 9C). Involvement of the β-subunit S108 autophosphorylation site in activation of AMPK has been reported recently (19), suggesting that the β-subunit may also come close to the kinase domain, consistent with our model (Fig. 9B,C). These effects would finally lead to the overall conformational change of the AMPK molecule as observed by SAXS in this work. According to this conformational switch model, the RS would not act as an autoinhibitory pseudosubstrate sequence inside the kinase domain loop, as for example in PKA and other protein kinases (see (72)), but rather contact the kinase domain at its backside as also proposed by Pang and colleagues (see Fig. 7 in (72)). Upon AMP binding to the γ-subunit, the RS relocates and thereby releases auto-inhibition (Fig. 9C). Please note that the structural part of the RS which supposedly would associate with the kinase domain, is not resolved in any of the published AMPK X-ray structures and thus structural information is not included in Fig. 9B.

Our model proposes that changes induced by AMP binding in the γ-subunit and transmitted via the RS sequence to the α-subunit may also alter accessibility of the phospho-T172 residue. This would make it less susceptible for dephosphorylation by protein phosphatase 2Cα (10,19), thus prolonging AMPK activation in presence of AMP (Fig. 9C). The entire process of AMP sensing and transmission of the conformational changes would lead to an overall compacting of the AMPK molecule as shown by SAXS (Figs 5 and 6) and depicted schematically in our model (Fig. 9C). The model integrates many old and recent findings, seems consistent with published data, and may give some new clues for further studies on the allosteric activation of AMPK.

Taken together, the quantitative results presented here shed new light on the molecular shape of native AMPK heterotrimer, at the resolution attainable by negative stain TEM methods and in-solution SAXS techniques. Overall, the molecular shape of AMPK particles was consistent irrespective of the method applied, suggesting that it reflects the "true" structural/functional state of mammalian AMPK at this resolution. The studies revealed a rapid concentration-dependent equilibrium between AMPK heterotrimers and defined dimers thereof. Finally, and most importantly, an AMP-induced conformational switch is shown to take place in full-length AMPK complex, suggesting a molecular mechanism for AMPK activation by allosteric activators. The techniques and results developed herein are expected to stimulate new and original approaches to pursue high-resolution structural characterization of full-length AMPK, as well as to aid a more detailed study of AMPK regulation *in vivo*.

FOOTNOTES

*Many thanks go to Ulrich Bauer (former Institute of Biotechnology, ETH Zurich) for introducing U.R. to the art of running large bioreactors, to Marco Gregorini (M.E. Müller Institute for Structural Biology, Basel) for his contributions to TEM microscopy, and to Sacnicte Ramirez (Inserm U884/ LBFA, UJF Grenoble) for assistance during the SAXS measurements at DESY, Hamburg. This work was supported by EU FP6 contract LSHM-CT-2004-005272 (EXGENESIS) and grants from the Swiss National Science Foundation (Nr. 3100AO-102075 to T.W. and U.S., Nr. 3100+0-11437/1 to T.W. and D.N. and Nr. 501 221 to A.E.), the French Agence Nationale de Recherche ("chaire d'excellence" given to U.S.), ETH Zurich (graduate training fellowship for R.S given to U.S. and T.W.), the Maurice E. Müller Foundation of Switzerland and the French Ministry of Education and Research (postdoctoral grant for U.R. given to U.S.). All members of the Wallimann group are acknowledged for help and discussion. Dmitri Svergun and Peter Konarev acknowledge support from the EU Design Study SAXIER, Contract No. 011934.

The abbreviations used are: AMPK, AMP activated protein kinase; CaMKK, Ca^{2+}/calmodulin-dependent protein kinase kinase; CBS, cystathionine beta synthase; DLS, dynamic light scattering; EM, electron microscopy; HPLC, high pressure liquid chromatography; IMAC, immobilized metal ion affinity chromatography; ITC, isothermal titration calorimetry; LKB1, serine/threonine kinase 11 (STK11); MALDI, matrix assisted laser desorption/ionization; MM, molecular mass; MO25, mouse protein 25; MS, mass spectrometry; PP2Cα, protein phosphatases-2C α isoform; RS, regulatory sequence; SAMS, synthetic peptide HMRSAMSGLHLVKRR; SAXS, small angle X-ray scattering; SNF1, carbon catabolite derepressing protein kinase; STEM, scanning transmission electron microscopy; STRAD, STE20-related adaptor protein; TEM, transmission electron microscopy; TMV, Tobacco mosaic virus; ToF, time of flight.

REFERENCES

1. Kahn, B. B., Alquier, T., Carling, D., and Hardie, D. G. (2005) *Cell Metab* **1**(1), 15-25
2. Hardie, D. G. (2007) *Nat Rev Mol Cell Biol* **8**(10), 774-785
3. Carling, D. (2005) *Biochimie* **87**(1), 87-91
4. Lee, J. H., Koh, H., Kim, M., Kim, Y., Lee, S. Y., Karess, R. E., Lee, S. H., Shong, M., Kim, J. M., Kim, J., and Chung, J. (2007) *Nature* **447**(7147), 1017-1020. Epub 2007 May 1017.
5. Neumann, D., Wallimann, T., Rider, M., Tokarska-Schlattner, M., Hardie, D. G., and Schlattner, U. (2007) Signaling by AMP-activated protein kinase. In: Saks, V. (ed). *Molecular System Bioenergetics - Energy for Life*, 1st Ed., Wiley-VCH, Weinheim, Germany
6. Hawley, S. A., Boudeau, J., Reid, J. L., Mustard, K. J., Udd, L., Makela, T. P., Alessi, D. R., and Hardie, D. G. (2003) *J Biol* **2**(4), 28
7. Shaw, R. J., Kosmatka, M., Bardeesy, N., Hurley, R. L., Witters, L. A., DePinho, R. A., and Cantley, L. C. (2004) *Proc Natl Acad Sci U S A* **101**(10), 3329-3335
8. Woods, A., Johnstone, S. R., Dickerson, K., Leiper, F. C., Fryer, L. G., Neumann, D., Schlattner, U., Wallimann, T., Carlson, M., and Carling, D. (2003) *Curr Biol* **13**(22), 2004-2008
9. Hawley, S. A., Pan, D. A., Mustard, K. J., Ross, L., Bain, J., Edelman, A. M., Frenguelli, B. G., and Hardie, D. G. (2005) *Cell Metab* **2**(1), 9-19
10. Suter, M., Riek, U., Tuerk, R., Schlattner, U., Wallimann, T., and Neumann, D. (2006) *J Biol Chem* **30**, 30
11. Hardie, D. G., and Carling, D. (1997) *Eur J Biochem* **246**(2), 259-273
12. Scott, J. W., Hawley, S. A., Green, K. A., Anis, M., Stewart, G., Scullion, G. A., Norman, D. G., and Hardie, D. G. (2004) *J Clin Invest.* **113**(2), 274-284.
13. Hardie, D. G., Hawley, S. A., and Scott, J. W. (2006) *J Physiol* **574**(Pt 1), 7-15
14. Xiao, B., Heath, R., Saiu, P., Leiper, F. C., Leone, P., Jing, C., Walker, P. A., Haire, L., Eccleston, J. F., Davis, C. T., Martin, S. R., Carling, D., and Gamblin, S. J. (2007) *Nature.* **449**(7161), 496-500. Epub 2007 Sep 2012.
15. McGilvery, R., and Murray, T. W. (1974) *J Biol Chem* **249**(18), 5845–5850

16. Hardie, D. G., and Hawley, S. A. (2001) *Bioessays* **23**(12), 1112-1119
17. Neumann, D., Schlattner, U., and Wallimann, T. (2003) *Biochem Soc Trans* **31**(Pt 1), 169-174
18. Schlattner, U., and Wallimann, T. (2004) Metabolite channeling: creatine kinase microcompartments. In: Lennarz, W. J., and Lane, M. D. (eds). *Encyclopedia of Biological Chemistry*, Academic Press, New York, USA
19. Sanders, M. J., Grondin, P. O., Hegarty, B. D., Snowden, M. A., and Carling, D. (2007) *Biochem J.* **403**(1), 139-148.
20. Iseli, T. J., Walter, M., van Denderen, B. J., Katsis, F., Witters, L. A., Kemp, B. E., Michell, B. J., and Stapleton, D. (2005) *J Biol Chem* **280**(14), 13395-13400
21. Wong, K. A., and Lodish, H. F. (2006) *J Biol Chem.* **281**(47), 36434-36442. Epub 32006 Sep 36429.
22. Hudson, E. R., Pan, D. A., James, J., Lucocq, J. M., Hawley, S. A., Green, K. A., Baba, O., Terashima, T., and Hardie, D. G. (2003) *Curr Biol* **13**(10), 861-866
23. Polekhina, G., Gupta, A., Michell, B. J., van Denderen, B., Murthy, S., Feil, S. C., Jennings, I. G., Campbell, D. J., Witters, L. A., Parker, M. W., Kemp, B. E., and Stapleton, D. (2003) *Curr Biol* **13**(10), 867-871
24. Warden, S. M., Richardson, C., O'Donnell, J., Jr., Stapleton, D., Kemp, B. E., and Witters, L. A. (2001) *Biochem J* **354**(Pt 2), 275-283
25. Hardie, D. G., and Sakamoto, K. (2006) *Physiology (Bethesda)* **21**, 48-60
26. Minokoshi, Y., Kim, Y. B., Peroni, O. D., Fryer, L. G., Muller, C., Carling, D., and Kahn, B. B. (2002) *Nature* **415**(6869), 339-343
27. Ruderman, N. B., Saha, A. K., and Kraegen, E. W. (2003) *Endocrinology* **144**(12), 5166-5171
28. Hardie, D. G. (2005) *Curr Opin Cell Biol* **17**(2), 167-173
29. Carretero, J., Medina, P. P., Blanco, R., Smit, L., Tang, M., Roncador, G., Maestre, L., Conde, E., Lopez-Rios, F., Clevers, H. C., and Sanchez-Cespedes, M. (2007) *Oncogene.* **26**(11), 1616-1625. Epub 2006 Sep 1614.
30. Andersson, Y., Le, H., Juell, S., and Fodstad, O. (2006) *Mol Cancer Ther* **5**(4), 1050-1059
31. Ashrafian, H. (2006) *Lancet* **367**(9510), 618-621
32. Luo, Z., Saha, A. K., Xiang, X., and Ruderman, N. B. (2005) *Trends Pharmacol Sci* **26**(2), 69-76
33. Bolster, D. R., Crozier, S. J., Kimball, S. R., and Jefferson, L. S. (2002) *J Biol Chem* **277**(27), 23977-23980
34. Dolinsky, V. W., and Dyck, J. R. (2006) *Am J Physiol Heart Circ Physiol.* **291**(6), H2557-2569. Epub 2006 Jul 2514.
35. Davies, J. K., Wells, D. J., Liu, K., Whitrow, H. R., Daniel, T. D., Grignani, R., Lygate, C. A., Schneider, J. E., Noel, G., Watkins, H., and Carling, D. (2006) *Am J Physiol Heart Circ Physiol* **290**(5), H1942-1951
36. Gollob, M. H. (2003) *Biochem Soc Trans* **31**(Pt 1), 228-231
37. Hardie, D. G. (2007) *Annu Rev Pharmacol Toxicol.* **47**, 185-210.
38. Rudolph, M. J., Amodeo, G. A., Bai, Y., and Tong, L. (2005) *Biochem Biophys Res Commun* **337**(4), 1224-1228
39. Nayak, V., Zhao, K., Wyce, A., Schwartz, M. F., Lo, W. S., Berger, S. L., and Marmorstein, R. (2006) *Structure* **14**(3), 477-485
40. Polekhina, G., Feil, S. C., Gupta, A., O'Donnell, P., Stapleton, D., and Parker, M. W. (2005) *Acta Crystallograph Sect F Struct Biol Cryst Commun* **61**(Pt 1), 39-42
41. Rudolph, M. J., Amodeo, G. A., Iram, S. H., Hong, S. P., Pirino, G., Carlson, M., and Tong, L. (2007) *Structure.* **15**(1), 65-74.
42. Day, P., Sharff, A., Parra, L., Cleasby, A., Williams, M., Horer, S., Nar, H., Redemann, N., Tickle, I., and Yon, J. (2007) *Acta Crystallogr D Biol Crystallogr.* **63**(Pt 5), 587-596. Epub 2007 Apr 2021.
43. Townley, R., and Shapiro, L. (2007) *Science.* **315**(5819), 1726-1729. Epub 2007 Feb 1728.
44. Amodeo, G. A., Rudolph, M. J., and Tong, L. (2007) *Nature.* **449**(7161), 492-495. Epub 2007 Sep 2012.
45. Neumann, D., Woods, A., Carling, D., Wallimann, T., and Schlattner, U. (2003) *Protein Expr Purif.* **30**(2), 230-237.

46. Neumann, D., Suter, M., Tuerk, R., Riek, U., and Wallimann, T. (2007) *Mol Biotechnol.* **36**(3), 220-231.
47. Bradford, M. M. (1976) *Anal Biochem.* **72**, 248-254.
48. Müller, S. A., Goldie, K. N., Bürki, R., Häring, R., and Engel, A. (1992) *Ultramicroscopy* **46**(1-4), 317-334
49. Müller, S. A., and Engel, A. (2001) *Micron* **32**(1), 21-31
50. Ludtke, S. J., Baldwin, P. R., and Chiu, W. (1999) *J Struct Biol.* **128**(1), 82-97.
51. Nazabal, A., Wenzel, J. R., and Zenobi, R. (2006) *Anal. Chem.* **78**(11), 3562 - 3570
52. Boulin, C. J., Kempf, R., Gabriel, A., and Koch, M. H. J. (1988) *Nucl. Instrum. Meth. A* **269**(1), 312-320
53. Roessle, M. W., Klaering, R., Ristau, U., Robrahn, B., Jahn, D., Gehrmann, T., Konarev, P., Round, A., Fiedler, S., Hermes, C., and D., S. (2007) *J. Appl. Cryst.* **40**, 190-194
54. Konarev, P. V., Volkov, V. V., Sokolova, A. V., Koch, M. H. J., and Svergun, D. I. (2003) *J. Appl. Crystallogr.* **36**, 1277-1282
55. Konarev, P. V., Petoukhov, M. V., Volkov, V. V., and Svergun, D. I. (2006) *J. Appl. Cryst.* **39**, 227-286
56. Guinier, A., and Fournet, G. (1955) *Small Angle Scattering of X-Rays*, Wiley, New York
57. Svergun, D. I. (1992) *J. Appl. Crystallogr.* **25**, 495-503
58. Porod, G. (1982). In: Glatter, O., and Kratky, O. (eds). *Small-angle X-ray scattering*, London
59. Svergun, D. I. (1999) *Biophys. J.* **76**(6), 2879-2886
60. Volkov, V. V., and Svergun, D. I. (2003) *J. Appl. Crystallogr.* **36**, 860-864
61. Treebak, J. T., Glund, S., Deshmukh, A., Klein, D. K., Long, Y. C., Jensen, T. E., Jorgensen, S. B., Viollet, B., Andersson, L., Neumann, D., Wallimann, T., Richter, E. A., Chibalin, A. V., Zierath, J. R., and Wojtaszewski, J. F. (2006) *Diabetes* **55**(7), 2051-2058
62. Xie, Z., Dong, Y., Zhang, M., Cui, M. Z., Cohen, R. A., Riek, U., Neumann, D., Schlattner, U., and Zou, M. H. (2006) *J Biol Chem* **281**(10), 6366-6375
63. Horman, S., Vertommen, D., Heath, R., Neumann, D., Mouton, V., Woods, A., Schlattner, U., Wallimann, T., Carling, D., Hue, L., and Rider, M. H. (2006) *J Biol Chem.* **281**(9), 5335-5340. Epub 2005 Dec 5339.
64. Baron, S. J., Li, J., Russell, R. R., 3rd, Neumann, D., Miller, E. J., Tuerk, R., Wallimann, T., Hurley, R. L., Witters, L. A., and Young, L. H. (2005) *Circ Res* **96**(3), 337-345
65. Carattino, M. D., Edinger, R. S., Grieser, H. J., Wise, R., Neumann, D., Schlattner, U., Johnson, J. P., Kleyman, T. R., and Hallows, K. R. (2005) *J Biol Chem* **280**(18), 17608-17616
66. Zou, M. H., Kirkpatrick, S. S., Davis, B. J., Nelson, J. S., Wiles, W. G. t., Schlattner, U., Neumann, D., Brownlee, M., Freeman, M. B., and Goldman, M. H. (2004) *J Biol Chem* **279**(42), 43940-43951
67. Taylor, E. B., Ellingson, W. J., Lamb, J. D., Chesser, D. G., Compton, C. L., and Winder, W. W. (2006) *Am J Physiol Endocrinol Metab* **290**(4), E661-669
68. Taylor, E. B., Ellingson, W. J., Lamb, J. D., Chesser, D. G., and Winder, W. W. (2005) *Am J Physiol Endocrinol Metab* **288**(6), E1055-1061
69. Svergun, D. I., Barberato, C., and Koch, M. H. J. (1995) *J. Appl. Crystallogr.* **28**, 768-773
70. Elbing, K., Rubenstein, E. M., McCartney, R. R., and Schmidt, M. C. (2006) *J Biol Chem* **281**(36), 26170-26180
71. Mitchelhill, K. I., Michell, B. J., House, C. M., Stapleton, D., Dyck, J., Gamble, J., Ullrich, C., Witters, L. A., and Kemp, B. E. (1997) *J Biol Chem* **272**(39), 24475-24479
72. Pang, T., Xiong, B., Li, J. Y., Qiu, B. Y., Jin, G. Z., Shen, J. K., and Li, J. (2007) *J Biol Chem* **282**(1), 495-506

TABLE LEGENDS

Table 1. Molecular properties of AMPK as determined by SAXS for two different AMPK isoform combinations at different concentrations. Abbreviations: *c*, protein concentration, D_{max}, maximal intramolocular distance, R_g, radius of gyration, MM, molecular mass, V_{Porod}, particle volume according to Porod.

Samples	c [mg/ml]	D_{max} [nm]	R_g [nm]	MM [kDa]	Porod Volume [nm^3]
$\alpha_2\beta_2\gamma_1$	0.52	16.0	4.64	140	230
$\alpha_2\beta_2\gamma_1$	1.92	16.0	4.84	141	254
$\alpha_2\beta_2\gamma_1$	13.18	28.0	7.62	215	445
$\alpha_2\beta_2\gamma_1$ with AMP	0.51	16.0	4.44	137	211
$\alpha_1\beta_1\gamma_1$	0.50	16.0	5.13	133	310
$\alpha_1\beta_1\gamma_1$	1.00	17.0	5.14	139	315
$\alpha_1\beta_1\gamma_1$	17.62	30.0	9.26	330	590
$\alpha_1\beta_1\gamma_1$ with AMP	0.98	16.0	4.92	136	288

FIGURE LEGENDS

FIGURE 1. **SDS-PAGEs and dynamic light scattering (DLS) of AMPK.** *A*. Coomassie Blue-stained SDS-PAGEs (12%), showing the purity of the full-length, untagged AMPK heterotrimeric isoforms purified with the 4-dimensional method described herein. Note: The β_2 chain shows anomalous electrophoretic migration behavior. *B*. DLS of two typical samples of concentrated $\alpha_2\beta_2\gamma_1$ AMPK (10 mg/ml) in SE2 buffer, showing a polydispersity of approximately 20%.

FIGURE 2. **Scanning transmission electron microscope (STEM) picture and mass determination of glutaraldehyde cross-linked $\alpha_2\beta_2\gamma_1$ AMPK.** *A*. Section of a STEM picture used for mass determination, scale bar = 50 nm. *B*. Histogram for the main medium size population of AMPK: 142, 232 $(\pm 33)^+$ kDa (n*~766, 154, respectively); the 142 kDa species corresponds to monomeric AMPK heterotrimers. *C*. Histogram for the smallest particles: 83, 130 $(\pm 21)^+$ kDa (n* ~36, 124, respectively), corresponding to partially dissociated AMPK complex species (83 kDa) or heterotrimers (130 kDa) *D*. Histogram for the largest particles: 221, 296, 392 $(\pm 28)^+$ kDa (n* ~52, 73, 17, respectively), with the 296 kDa species corresponding to the dimer of heterotrimers). *The values of n are approximate and are measured between the points of peak overlap. $^+$The standard deviations are within the size expected from background fluctuations.

FIGURE 3. **High-mass MALDI spectra of heterotrimeric $\alpha_2\beta_2\gamma_1$ AMPK complex and single-subunits.** *A*. Overlay spectra of AMPK complex analyzed before cross-linking (black trace) clearly showing the mass of the single-subunits (30,24 kDa for β_2 37.38 kDa for γ_1 and 62.26 kDa for α_2) and after cross-linking (red trace) showing intact $\alpha_2\beta_2\gamma_1$ complex (129.95 kDa). *B*. Subtraction spectrum obtained by subtracting the control spectrum from the cross-linked spectrum. It reveals the predominance of the heterotrimer complex $[\alpha_2\beta_2\gamma_1]$ with m/z=129.95. Note that the peak at 64.97 kDa corresponds to the doubly charged heterotrimer ion $[\alpha_2\beta_2\gamma_1]^{+2}$

FIGURE 4. **Electron microscopy of negatively stained $\alpha_2\beta_2\gamma_1$ AMPK.** The scale bar corresponds to 50 nm. The insets display the averaged images of the major classes of a total of 937 hand picked images, representing different orientations of the particle on the carbon support. The inset baselines each correspond to 18 nm.

FIGURE 5. **Small angle X-ray scattering curves of AMPK in solution.** The log10 of the radially symmetric scattered X-ray intensity around *I(0)* is plotted as a function of the momentum transfer *s*. Large congruence of the scattering curves from $\alpha_1\beta_1\gamma_1$ AMPK in diluted solution of 1,00 mg/ml (blue) and 0.50 mg/ml (red), after scaling to the protein concentration. This indicates that no further decrease of maximum size and radius of gyration of AMPK particles occurs within this protein concentration range. *B*. Diluted, monodisperse AMPK solutions of $\alpha_1\beta_1\gamma_1$ (without AMP magenta; with AMP green) and $\alpha_2\beta_2\gamma_1$ (without AMP blue; with AMP red), showing a small but significant change upon AMP ligand binding.

FIGURE 6. **SAXS curves of AMPK isoforms and corresponding distance distribution functions.** Scattering curves in *A* and distance distribution functions in *B*. at different concentrations show the effect of concentration dependent reversible dimerization of AMPK heterotrimers. Scattering curves 4-6 are scaled by a factor 10 for graphical comparison. 1-3: $\alpha_2\beta_2\gamma_1$ AMPK 1- high concentration (13 mg/ml), 2- low concentration (0.4 mg/ml), 3- low concentration (0.4 mg/ml) + AMP. 4-6: $\alpha_1\beta_1\gamma_1$ AMPK 4- high concentration (17.6 mg/ml), 2- low concentration (0.8 mg/ml), 3- medium concentration (2.2 mg/ml) + AMP.

FIGURE 7. **Gallery of selected views from an individual $\alpha_1\beta_1\gamma_1$ AMPK model without AMPK ligand.** The model demonstrates the similarity to the single particle TEM averages of AMPK. The diameter of the spheres is 8.5 Å.

FIGURE 8. **Gallery of averaged, filtered DAMMIN models of $\alpha_2\beta_2\gamma_1$ AMPK**, Each model was obtained by DAMAVER software, based on 10 individual models of each ±AMP. Green: $\alpha_2\beta_2\gamma_1$ AMPK without AMP, the cut-off volume is $2.440 \bullet 10^5$ Å^3. Red: $\alpha_2\beta_2\gamma_1$ apo AMPK with AMP, the cut-

off volume is $2.209 \bullet 10^5$ Å^3. Note: The diameter of the spheres building the space models is 8.5 Å for the green and 7.4 Å for the red model. *A1* and *A2*. Two different views of the averaged models of $\alpha_2\beta_2\gamma_1$ AMPK ± AMP shown superimposed, centered on the center of mass and oriented along their axis of inertia. *B*. $\alpha_2\beta_2\gamma_1$ AMPK with AMP approximately in the same orientation as in A2. *C*. $\alpha_2\beta_2\gamma_1$ apo AMPK without AMP approximately in the orientation as in A2.

FIGURE 9. **Model for AMPK activation by AMP: a novel role for the regulatory sequence.**
The model is mainly based on the recent X-ray structure of the *S. cerevisiae* AMPK ortholog core complex (44). Crystallized parts of the sequence are shown in color: *red*, C-terminus plus regulatory sequence (RS) of the α-subunit; *green*, C-terminus plus glycogen binding domain (GBD) of the β-subunit; *blue*, complete γ-subunit with the AMP-binding CBS domains. Bound AMP and ATP are in *magenta* or *white*, respectively. Sequence sections lacking corresponding structural information are in *grey*: e.g. kinase domain (KD) with activation loop (AL) of the α-subunit and a significant N-terminal part of the β-subunit
A. Domain organization of *S. cerevisiae* AMPK ortholog. Snf1, Sip2 and Snf4 correspond to α-, β- and γ-subunits, respectively, of mammalian AMPK (amino acid numbering according to *S. cerevisiae*, modified after (44)).
B. Structural model of a putative full-length AMPK complex. The structure of the core complex of *S. cerevisiae* AMPK ortholog (PDB:2QLV) is turned sidewise by 90° relative to the representations in Amodeo et al. (44). Three AMP molecules (one fixed, two exchangeable,) were introduced by superposition with the very homologous core structures of mammalian AMPK using PDB:2V8Q (see also suppl. Fig. 1). The α-subunit KD (Littler et al. 2006, Structural Genomics Consortium, PBD:2H6D) was added to its putative location (see Fig 1B in (43)), in close proximity to the α-subunit RS and with the active site pointing to the outside of the complex. Some part of the RS, including the autoinhibitory domain with a conserved putative α-helix, is not resolved in any of the known X-ray structures. The autoinhibitory domain was proposed to bind to the backside of the small lobe of the KD (72). Note: The RS is sandwiched in-between the γ-subunit (*blue*), with its AMP binding sites, and the KD (*grey*). This would allow the RS to mediate a cross-talk between AMP binding sites and the KD or other parts of the AMPK complex as outlined in *C*.
C. Simplified model for the mechanism of AMPK regulation by AMP. This model is based on the putative structure of AMPK (shown in *B*) and incorporates data from us (this work and (10)), as well as others (e.g. (43,72)). The (P) in the KD indicates the activatory phosphorylation at T172 (6-9). **Left**: At low AMP/ATP ratio, binding sites 1 and 2 are occupied by ATP and site 3 by non-exchangeable AMP. The T172-phosphate group is easily accessible to protein phosphatase 2Cα for dephosphorylation (10,19), resulting in low AMPK activity. **Right**: At increasing AMP/ATP ratio, replacement of ATP by AMP at the reversible AMP-binding sites 1 and/or 2 would result in small conformational changes and/or changes in surface potential of the γ-subunit (43). Given the structure outlined in *B*, our model proposes transmission and amplification of these changes by the neighboring RS and KD (small open arrows) leading to release of autoinhibition of the KD by retracting the RS and pulling the KD domain closer to the core of the AMPK molecule. The overall compaction of the heterotrimer is interpreted in our model as a movement of RS (red arrow) and KD (black arrow), as well as a conformational change in the KD. The latter would protect phospho-T172 against dephosphorylation, thus keeping AMPK in its phosphorylated, active form.

FIGURE LEGENDS (supplemental data)

Suppl. FIGURE 1. **X-ray structure of the truncated AMPK ortholog of *S.cerevisiae*** (modified from (44); PBD 2QLV).
Color code according to Fig. 10: *red*, α-subunit, including the regulatory sequence (RS) lying on top of the γ-subunit; *green*, β-subunit, including the glycogen binding domain (GBD), and *blue*, the complete γ-subunit. The three AMP molecules (bound at AMP binding sites 1-3) that were not present in the Amodeo et al. X-ray structure have been introduced here by superposition with the very homologous X-ray structure of truncated mammalian AMPK ((14); PDB: 2V8Q), where three bound AMP molecules were present. One is a tightly bound, unexchangeable AMP (fixed AMP at site 3) and two are exchangeable AMPs (sites 1 and 2), working as actual AMP sensors. Snf1, Sip2 and Snf4 of the yeast ortholog correspond to the α-, β-, and γ-subunits, respectively, of mammalian AMPK.

Suppl. FIGURE 2. **Automated 4-dimensional purification of AMPK and activity.**
A, Chromatogram of the entire automated 4-dimensional procedure for $\alpha_1\beta_1\gamma_1$ AMPK. The high absorption until 200 ml indicates the load and wash of the first column (Ni-IDA) and elution around 300 ml, followed by loading and washing of the second column (Red Sepharose) and elution at around 600 ml. To concentrate AMPK, this eluate is loaded onto the third column (2 ml Ni-HP crude) and eluted around 800 ml. During the following 240 ml, the fourth column (size exclusion) is equilibrated while the sample is incubating in the super loop. Au, absorbance units. *Insert:* Magnification of the AMPK elution peak from the size exclusion column. *B*, Histogram of specific AMPK activities (hatched bars) and protein concentrations (solid black bars) of individual fractions of the second size exclusion chromatography run.

Figure 1

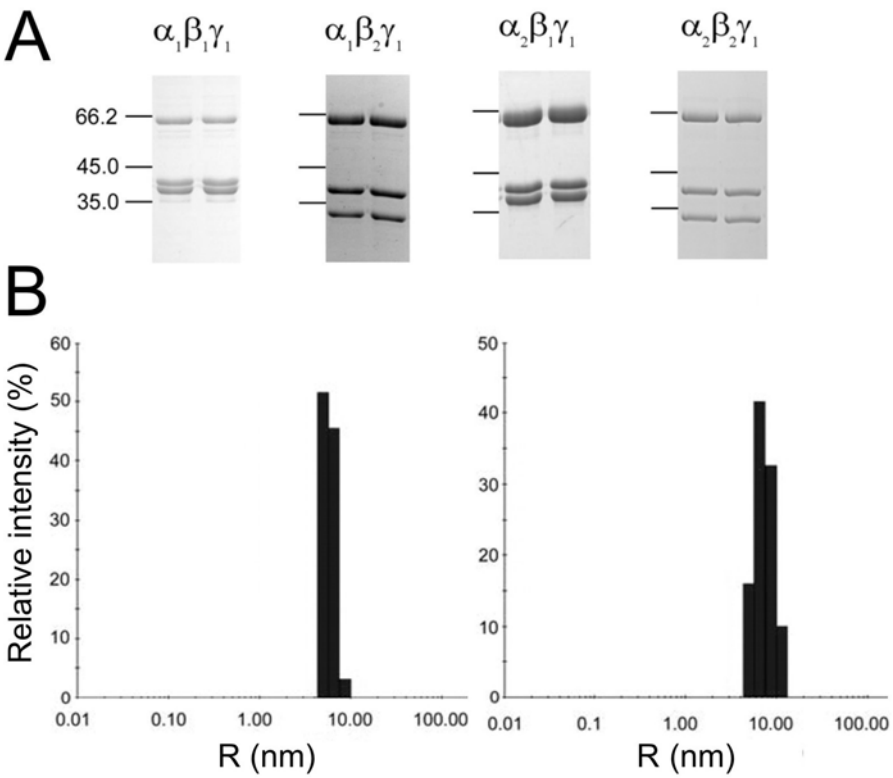
A
α1β1γ1
α1β2γ1
α2β1γ1
α2β2γ1
66.2
45.0
35.0
B
Relative intensity (%)
R (nm)
R (nm)

Figure 2

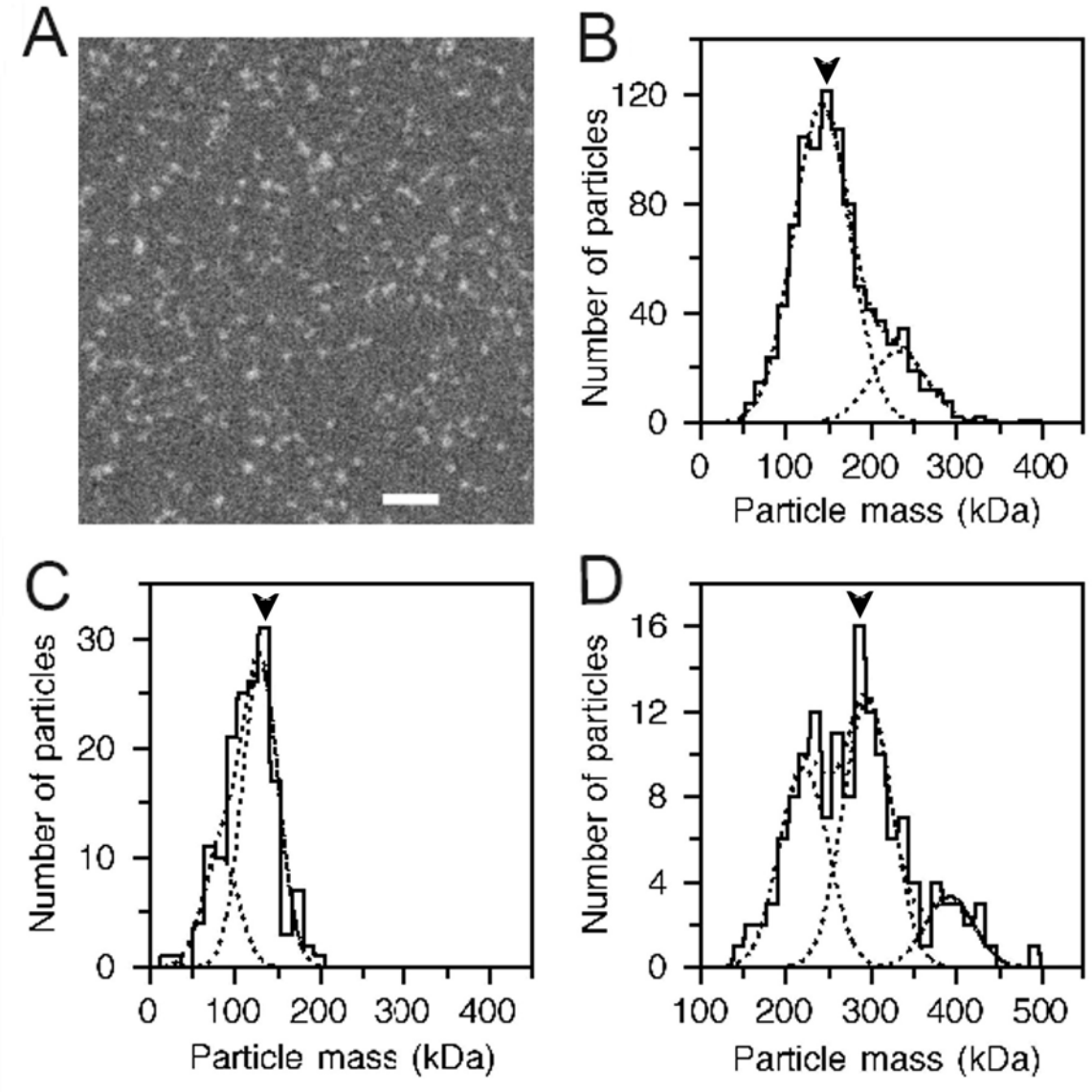
A
B
Number of particles
120
80
40
0
0 100 200 300 400
Particle mass (kDa)
C
Number of particles
30
20
10
0
0 100 200 300 400
Particle mass (kDa)
D
Number of particles
16
12
8
4
0
100 200 300 400 500
Particle mass (kDa)

Figure 3

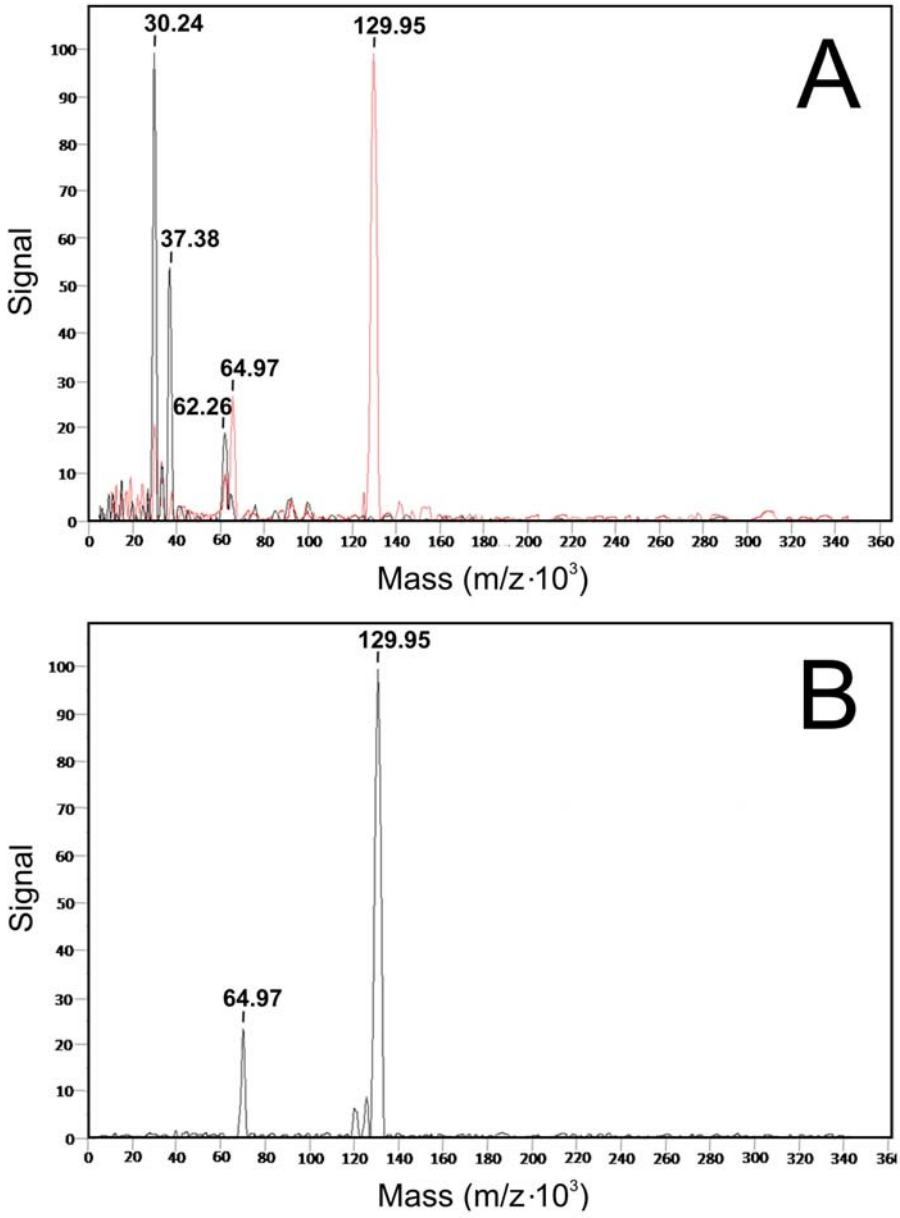
A
30.24
129.95
37.38
64.97
62.26
Signal
Mass (m/z·10³)
B
129.95
64.97
Signal
Mass (m/z·10³)

Figure 4

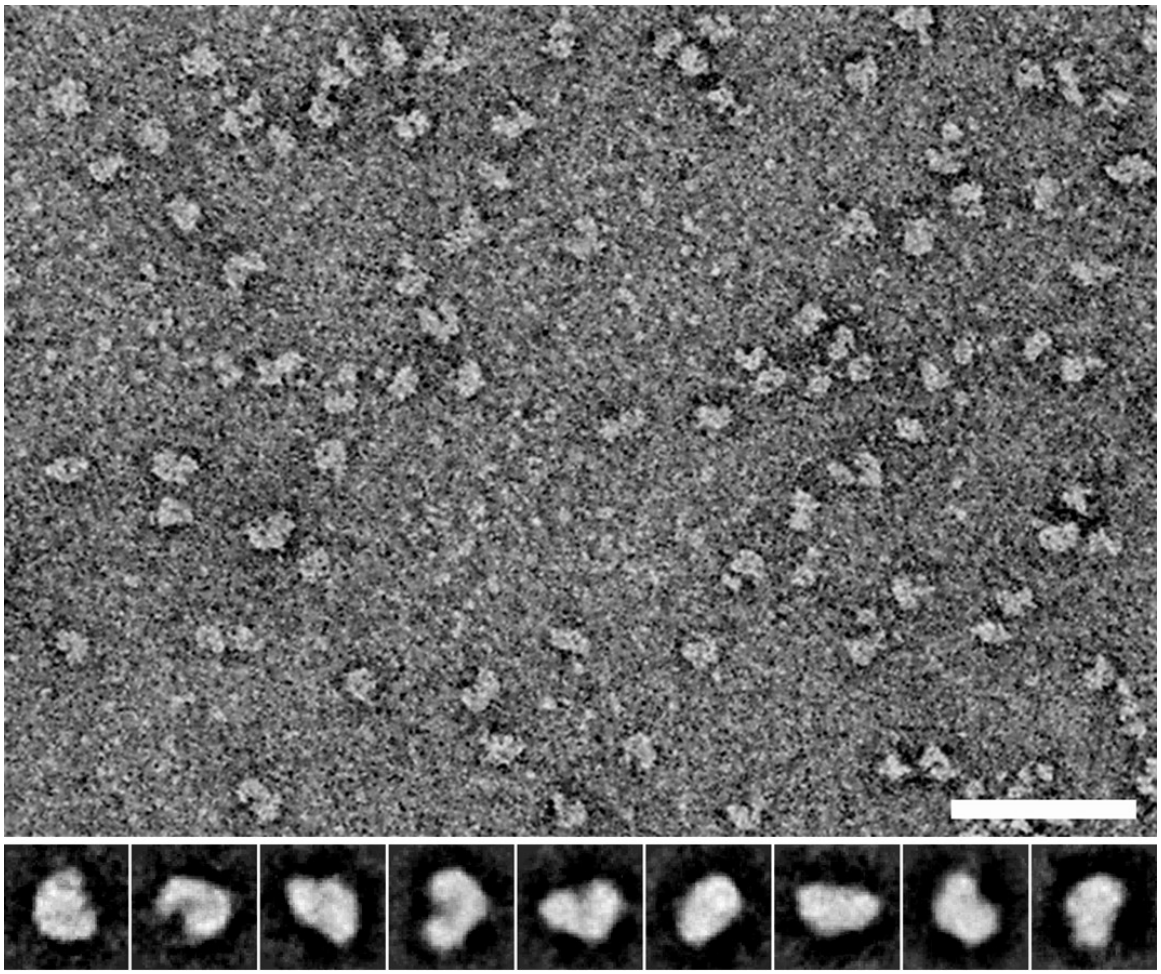

Figure 5

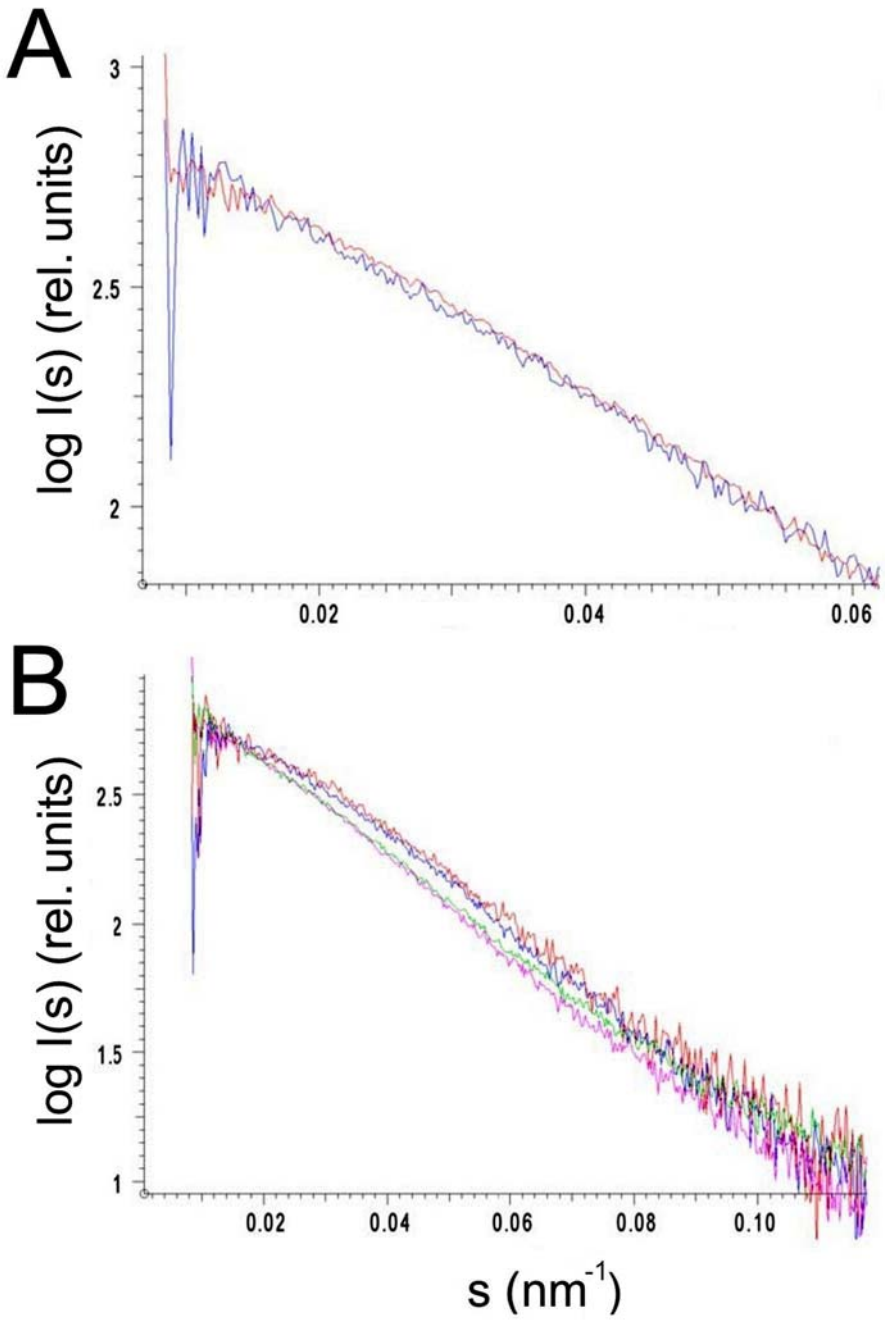
A
log I(s) (rel. units)
3
2.5
2
0.02
0.04
0.06
B
log I(s) (rel. units)
2.5
2
1.5
1
0.02
0.04
0.06
0.08
0.10
s (nm-1)

Figure 6

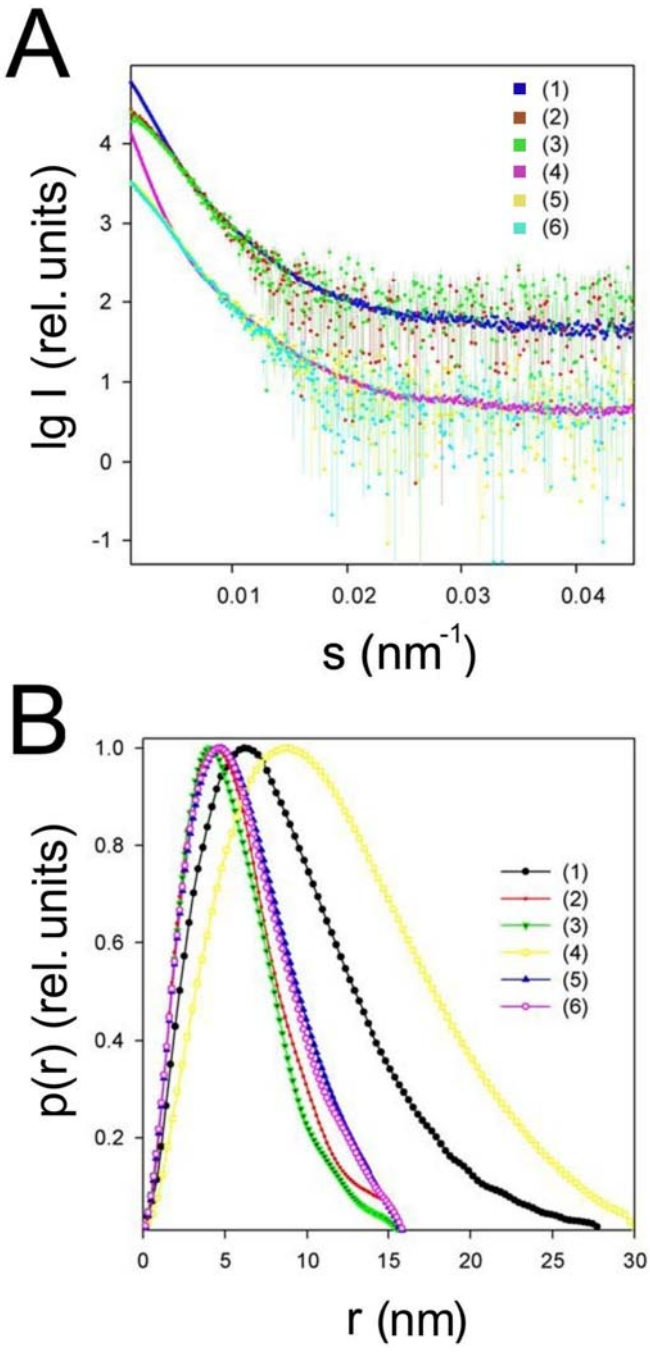

Figure 7

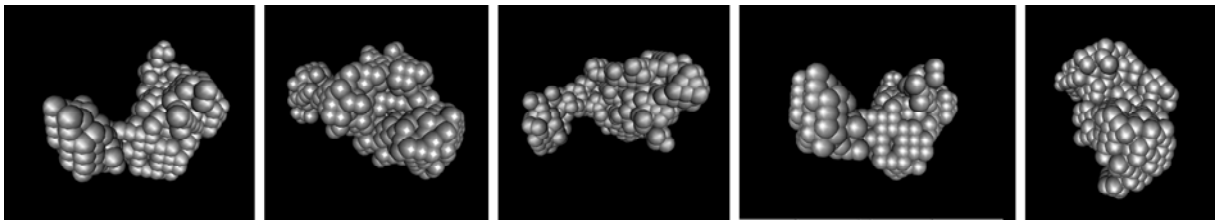

Figure 8

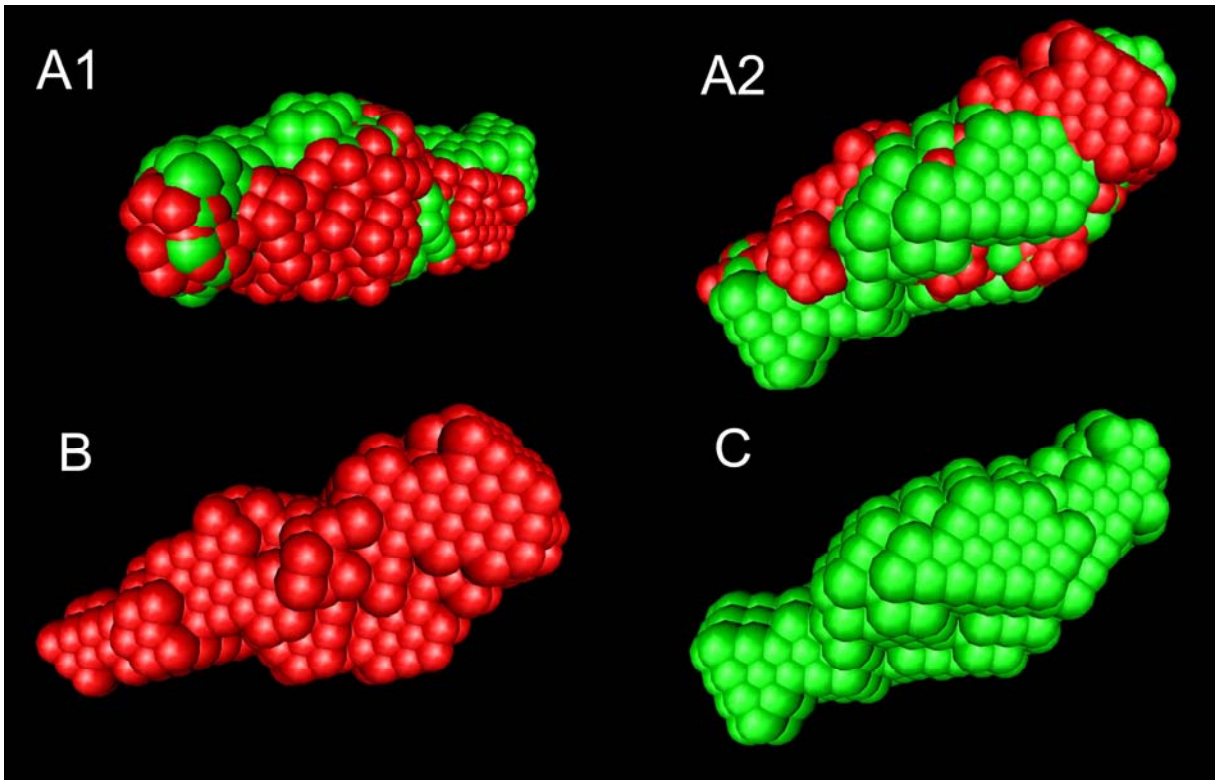

Figure 9

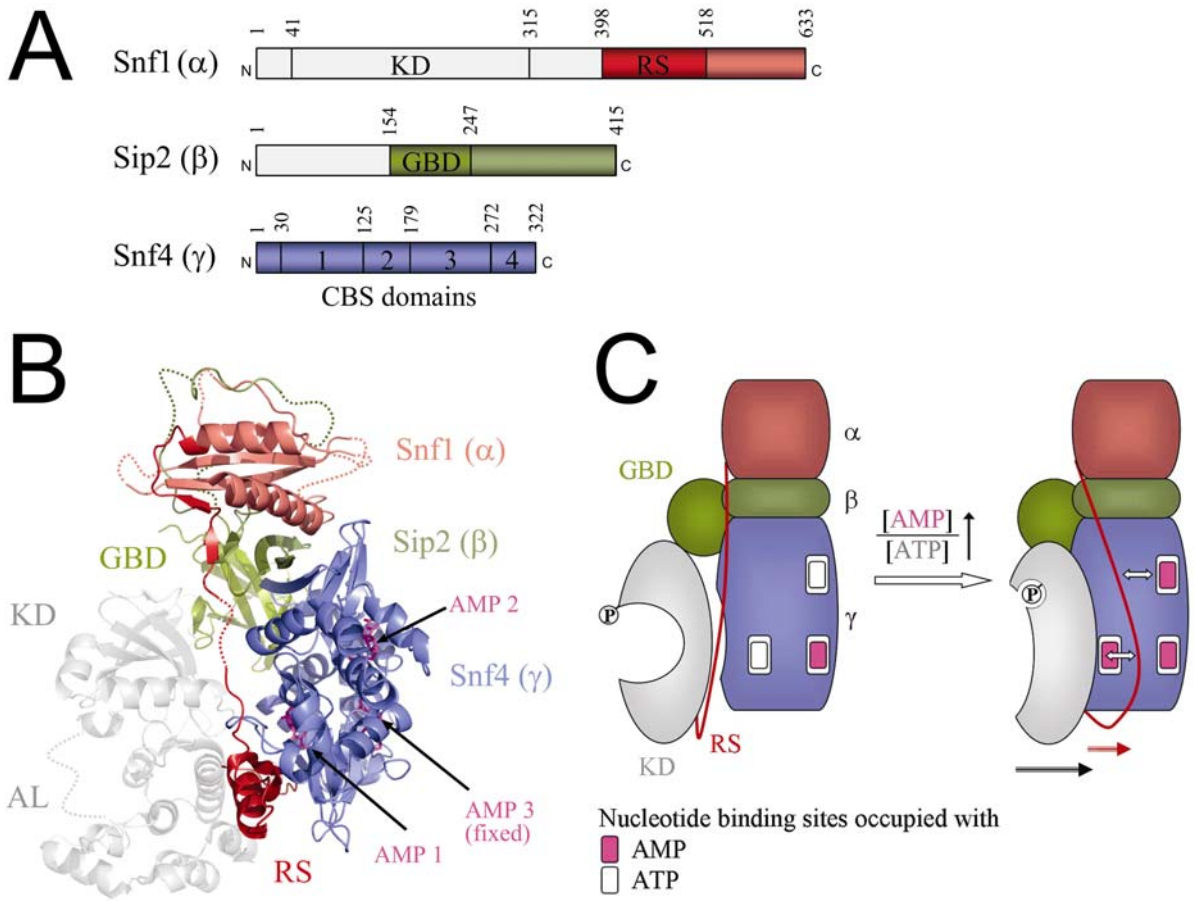
A
Snf1 (α)
1
41
315
398
518
633
N
KD
RS
C
Sip2 (β)
1
154
247
415
GBD
Snf4 (γ)
1
30
125
179
272
322
1
2
3
4
CBS domains
B
Snf1 (α)
Sip2 (β)
GBD
KD
AMP 2
Snf4 (γ)
AL
AMP 3
(fixed)
AMP 1
RS
C
GBD
α
β
γ
[AMP]
[ATP]
P
RS
KD
Nucleotide binding sites occupied with
AMP
ATP

Suppl. Figure 1

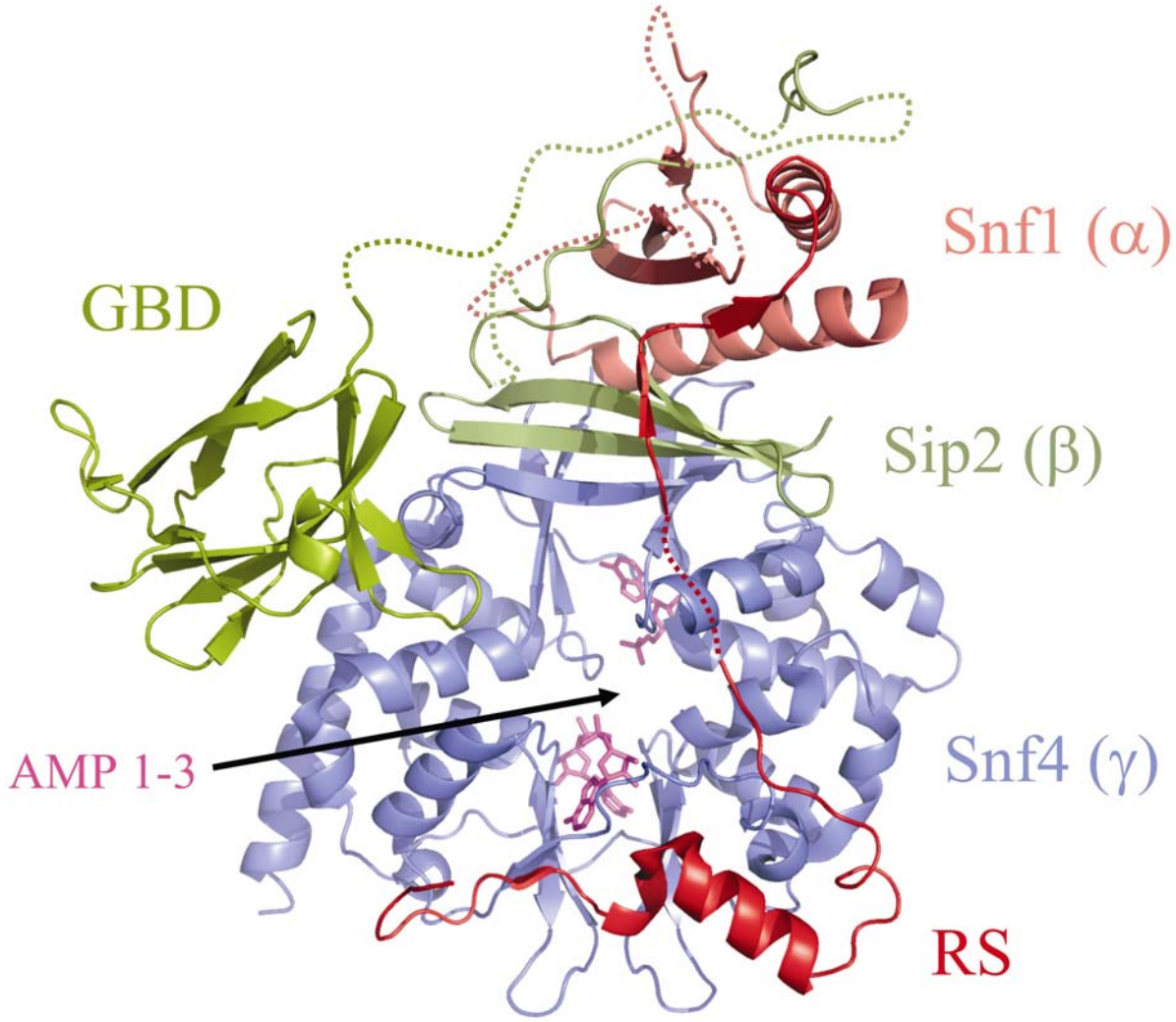

Suppl. Figure 2